Politecnico di Torino

Politecnico di Torino

Electronic Engineering

Electronic engineering, Telecommunications and Physics department

Radio Frequency Systems Design

April 2024

Multiport double layer nearfield geodesic lens antenna in V band

SUPERVISORS

Prof. Ladislau Matekovits

Prof. Oscar-Quevedo Teruel

CANDIDATE

Valerio Mannocchi

A mio nonno Sergio

ABSTRACT

The continuous demand for high data rate communication links is a state-of-the-art in nowadays 5G mobile networks. Millimeter-wave (mmWave) is highly attractive for performing data transmission due to the available bandwidth at such high frequency band. In order to relieve the free space path loss, high gain antennas are required as well as improved coverage characteristics for users within the field of view of interest. As a consequence, reliable 5G point to multipoint communication require stable aggregate gain in the farfield with low roll-off at crossover points between adjacent beams. Previous works based on lenses or quasi optical systems in the mmWave band such as Ruze lenses, Rotman lenses and Luneburg lenses are not suitable to fulfill this requirement. Due to their farfield focusing property, they produce very narrow pencil beams thus resulting in poor performance in terms of beam coverage. A roll-off greater than 3 dB between adjacent beams and an half power beam width (HPBW) smaller than $20°$ is obtained. As a consequence, reliability of communication is reduced over the angular area of interest. In order to guarantee stable aggregate gain characteristics, a novel approach is proposed in this Master Thesis based on defocusing property of a multiport double layer nearfield geodesic lens antenna in the 56-62 GHz frequency band (V band). Here the nearfield property is exploited to widen the beams in farfield, thus increasing dramatically the HPBW and reducing the roll-off between them. As a first analysis , the design and optimization of a single port double layer nearfield geodesic lens has been reported. Furthermore, a five-port multibeam double layer nearfield geodesic lens has been designed and simulated as a final case of study. Analytical rigorous formulation aided by CAD tools has been pursued to derive and optimize the geodesic lens profile according to the design requirements. An initial theoretical lens profile has been derived from differential equation resulting in degraded antenna coverage over the angular sector of interest. Indeed, an HPBW smaller than 20° and roll-off equal to 7 dB between adjacent beams has been obtained in the 56-62 GHz band. As a consequence, an optimization on lens profile has been carried out to improve beam coverage capability. The main novelty of the final optimized multiport lens is to achieve an HPBW greater than 20° and a roll off smaller than 3 dB at crossover points between adjacent beams thus resulting in a stable aggregate gain in 56-62 GHz band. The lens scanning region is equal to $\pm 55°$ in the H

plane thus allowing no degradation in link performance for users in this sectorial area. Multibeam radiation pattern results have been validated in the frequency band of interest. Furthermore, the absolute value and phase of electric field when feeding different ports have been also analyzed thus showing the nearfield focusing property of such lens antenna. As final consideration, scattering parameters when different ports being fed have been reported for complete analysis.

CONTENTS

1 Introduction **11**
1.1 Motivation 11
1.2 Description of the problem 12
1.3 Thesis structure 13
2 Theory **14**
2.1 Reflection and refraction theory 14
2.2 Fresnel formulae 16
2.3 Basic principle of lenses and homogenous lenses 17
2.4 Graded index lenses 18
2.4.1 Luneburg lens 19
2.5 Single layer geodesic lenses 21
2.5.1 Motivation 21
2.5.2 Analytical derivation 22
2.6 Double layer geodesic lenses 27
2.6.1 Motivation 27
2.6.2 Analytical derivation 28
3 Double layer nearfield geodesic lens antenna **32**
3.1 Design and methodology 32
3.2 Design parameters 34
3.3 Mirror 35
3.4 Flare 37
3.5 Feeding 38
3.6 Single port double layer lens layout and results 41
3.7 Optimization of double layer nearfield geodesic lens profile 44
3.8 Optimized single port double layer lens layout and results 46
3.9 Multiport double layer lens layout and results 55
4 Conclusion and future work **64**

LIST OF FIGURES

Figure 1 Incident, reflected and transmitted waves 14

Figure 2 Lens antenna exploited in reception (a) and transmission (b) 17

Figure 3 Propagation of rays in a Luneburg lens antenna [11] 19

Figure 4 Beam scanning in terms of rays in a Luneburg Lens [12] 20

Figure 5 Relationship between physical length and optical path (graded $\eta(r)$ and uniform $\eta_0 = 1$) 22

Figure 6 Graded index lens [16] (a) and geodesic lens [16] (b) 22

Figure 7 Geodesic height $z(\rho)$ vs ρ in Luneburg and nearfield Lenses 25

Figure 8 3D vacuum model of a single-feed nearfield geodesic lens antenna ($r_1 = 1$, $r_2 = 2$) (a) and cross section view (b) 26

Figure 9 Double layer gradient refractive index lens in a polar coordinate system (r, φ) (a) [19] and its geodesic equivalence in a cylindrical coordinate system (ρ, φ, z) (b) [19] 29

Figure 10 Comparison between lens profile derived from differential equation (14) and approximation curve based on super ellipse formulation 34

Figure 11 Central and inner and outer profiles with PPW region of the nearfield double layer geodesic lens. The mirror and chamfer feeding are also included in the plot 35

Figure 12 Reflection coefficient of the mirror (a). The mirror has an height $h_{mir} = 0.8\ mm$ and a length $l_{mir} = 0.8\ mm$ (b) 36

Figure 13 Reflection coefficient of the flare (a). The flare has an height $h_f = 5\ mm$ and a length $l_f = 8.75\ mm$ (b) 38

Figure 14 Metal (a) and air part (b) of stepped horn transition. A cross section view of the metal part is also included with stepped horn parameters (c) 39

Figure 15 Simplified model for S_{11} optimization. Perspective (a) and side view (b) 39

Figure 16 Reflection coefficient S_{11} at transition between stepped horn and lens profile 40

Figure 17 Perspective view metal part (a) of double layer lens antenna and cross section view (b) 41

Figure 18 Perspective view air part (a) of double layer lens antenna and cross section view (b) 41

Figure 19 Farfield patterns at $f_{min} = 56$ GHz, $f_c = 60$ GHz, $f_{max} = 62$ GHz 42

Figure 20 S_{11} reflection coefficient including full model and simplified model of Figure 16 43

Figure 21 Initial lens profile from (23) and optimized lens profile from (24) 45

Figure 22 Central and inner and outer profiles with PPW region for both the initial lens design and optimized one. In this plot both the flare and stepped horn are not shown 45

Figure 23 Radiation patterns including the initial lens profile and optimized lens profile 47

Figure 24 Absolute value of $\vec{E}$ at 56 GHz. Perspective view (a) and bottom view (b) of the lens model are included 49

Figure 25 Absolute value of $\vec{E}$ at 60 GHz. Perspective view (a) and bottom view (b) of the lens model are included 50

Figure 26 Absolute value of $\vec{E}$ at 62 GHz. Perspective view (a) and bottom view (b) of the lens model are included 51

Figure 27 Phase of $\vec{E}$ at 56 GHz. Perspective view (a) and bottom view (b) of the lens model are included. 52

Figure 28 Phase of $\vec{E}$ at 60 GHz. Perspective view (a) and bottom view (b) of the lens model are included 53

Figure 29 Phase of $\vec{E}$ at 62 GHz. Perspective view (a) and bottom view (b) of the lens model are included 54

Figure 30 Comparison between S_{11} reflection coefficient of both the initial lens profile and the optimized lens profile 55

Figure 31 Perspective view metal part (a) of double layer lens antenna and cross section view (b) 56

Figure 32 Perspective view air part (a) of double layer lens antenna and top view (b) 56

Figure 33 Radiation patterns at 56 GHz when all ports being fed both for the initial lens profile (dashed lines) and optimized lens profile (solid line) 57

Figure 34 Radiation patterns at 60 GHz when all ports being fed both for the initial lens profile (dashed lines) and optimized lens profile (solid line) 58

Figure 35 Radiation patterns at 62 GHz when all ports being fed both for the initial lens profile (dashed lines) and optimized lens profile (solid line) 58

Figure 36 Absolute value of $\vec{\mathrm{E}}$ at 56 GHz bottom view when Port1 (a) and Port3 (b) being fed 59

Figure 37 Absolute value of $\vec{\mathrm{E}}$ at 60 GHz bottom view when Port1 (a) and Port3 (b) being fed 59

Figure 38 Absolute value of $\vec{\mathrm{E}}$ at 62 GHz bottom view when Port1 (a) and Port3 (b) being fed 60

Figure 39 Phase of electric field $\vec{\mathrm{E}}$ at 56 GHz bottom view when Port1 (a) and Port3 (b) being fed 60

Figure 40 Phase of electric field $\vec{\mathrm{E}}$ at 60 GHz bottom view when Port1 (a) and Port3 (b) being fed 61

Figure 41 Phase of electric field $\vec{\mathrm{E}}$ at 62 GHz bottom view when Port1 (a) and Port3 (b) being fed 61

Figure 42 Reflection coefficient when Port1-5 being fed 62

Figure 43 S-Parameters when Port3 being fed 62

Figure 44 S-Parameters when Port1 being fed 63

LIST OF TABLES

Table 1 Design requirements 32

Table 2 Optimal values of stepped horn parameters 40

Table 3 Farfield results at $f_{min} = 56\ GHz, f_c = 60\ GHz, f_{max} = 62\ GHz$ 42

Table 4 Farfield results at $f_{min} = 56\ GHz, f_c = 60\ GHz, f_{max} = 62\ GHz$ for both the initial lens profile and optimized lens profile.....47

ACRONYMS

η	Refractive index
ε_r	Relative permittivity
μ_r	Relative permeability
ξ	Characteristic impedance
θ	Theta angle
φ	Phi angle
λ	Wavelength
υ	Propagation constant
$\mathbf{E}$	Electric field
$\mathbf{A}$	Electric potential vector
Γ	Reflection coefficient
$\mathbf{T}$	Transmission coefficient
ρ	Normalized radial coordinate cylindrical coordinate system
$\mathbf{r}$	Normalized radial coordinate polar coordinate system
$\mathbf{s}$	Meridian length
$\mathbf{z}$	Height of the lens profile
$\mathbf{h_0}$	Maximum normalized height of the lens
$\mathbf{p}$	Lens parameter super ellipse equation
$\mathbf{q}$	Lens parameter super ellipse equation
σ	Optical path
$\mathbf{L}$	Angular momentum
$\mathbf{R}$	Radius of the lens
mmWave	Millimeter wave band

LEO	Low Earth Orbit
SIW	Substrate integrated waveguide
PPW	Parallel plate waveguide
TEM	Transverse electromagnetic
HPBW	Half-power beam width
SLL	Side lobe level
PEC	Perfect electric conductor
CST	CST studio suite
PMC	Perfect magnetic conductor
WR19	Standard rectangular waveguide
a	Width of rectangular waveguide
b	Height of rectangular waveguide

1 INTRODUCTION

1.1 MOTIVATION

The new mobile cellular network generations, such as 5G, require incredibly high data rates to guarantee fast and reliable multimedia streaming and services over a wide sectorial coverage [1]. The need for such high speed stream of data requires working at higher frequency towards the millimeter-wave band (mmWave) [2] in order to increase the available bandwidth.

However, from the Friis formula, it is clear that increasing the bandwidth and so transmitting at higher frequencies results in an increase of free space path loss. Therefore highly directive antennas are required to relieve propagation loss as well as feeding network losses. The main candidates to be considered are planar array antennas [3], reflector antennas or reflectarrays [4] and lens antennas [5].

In this Master Thesis a focus is done on lens antennas since the lens solution is particularly interesting with respect to the other solutions previously mentioned due to the fact that, with lenses, beam scanning is achievable over a wide angular range without ideally any scan losses (that instead arise with reflector antennas and planar array antennas).

Nowadays lens antennas based solution is mainly exploited at high frequency bands and Sub THz applications. The main fields of application are satellite communications for LEO, 5G communications and automotive and surveillance Radar applications where fully metallic lenses such as geodesic lenses are exploited to overcome losses in the dielectric materials.

1.2 DESCRIPTION OF THE PROBLEM

The new mobile 5G communications require very high link performance over a wide sectorial coverage at high frequencies. For this purpose, stable aggregate gain is needed in the farfield over a wide angular range for point-to-multipoint communications. Wider beams in farfield and low roll-off at crossover points between adjacent beams are possible solutions for such purposes.

Lenses or quasi optical systems in the mmWave band previously studied such as Ruze lenses [6], Rotman lenses [7] and Luneburg lenses [8] are not suitable to fulfill this requirement. Due to their farfield focusing property and feeding separation between the ports, they produce very narrow pencil beams with crossover points between two adjacent beams 7 dB below the maximum value of the main beam.

This results in strong variations of the gain in farfield in the considered sectorial coverage for communication and thus in variation of the link communication performance. A study in the past [9], by defocusing a Luneburg lens and make it focusing in the nearfield, led to wider beams in the farfield thanks to the use of nearfield geodesic lens antenna made of just one single layer.

Starting from that work [9], a stable aggregate gain (with a roll-off lower than 3 dB) is achieved in this Master Thesis at higher frequencies in 56-62 GHz band by means of a multiport double layer nearfield geodesic lens antenna. The scanning range achieved is $\pm 55°$ in the H plane.

1.3 THESIS STRUCTURE

The outline of this Master Thesis is here proposed:

- In Chapter 2, after introducing geometrical optics theories on reflection and refraction , lens antenna background is reported. In section 2.3, the basic principle of homogenous dielectric lenses is discussed. Graded index lenses (2.4) and , as a specific case, Luneburg lens (2.4.1) are also analyzed. Single layer (2.5) and double layer (2.6) geodesic principles are discussed thoroughly as a final consideration.

- In Chapter 3, the case of study of this Master Thesis is reported that is the double layer nearfield geodesic lens antenna. Single port solution is analyzed in terms of design parameters (3.1-3.3) of each component of the lens. First, initial lens profile results (3.4) have been discussed and further optimization (3.5-3.6) is explained. A comparison between the two is reported as well.

- In Chapter 4, the multiport double layer nearfield geodesic lens is discussed as a final design. Radiation pattern results have been showed as well as electric field contour plots in terms of absolute value and phase in the frequency band of interest. S-parameters have been discussed as well.

- In Chapter 5, conclusion and future work is reported.

2 THEORY

A lens antenna is an antenna that exploits a dielectric or metal lens to change the ray trajectory of electromagnetic waves. For such purpose, lens antennas are considered a particular case of aperture antennas. As a consequence, they are large devices in terms of wavelength λ so that can be first designed and analyzed by exploiting ray or geometrical optics, based on reflection and refraction theory. As a final formulation, physical theory and full wave analysis with Fresnel Formulae are applied.

2.1 REFLECTION AND REFRACTION THEORY

Consider two media with two different refractive indexes η_1 and η_2 and consider an incident wave S_i coming from the medium with refractive index η_1.

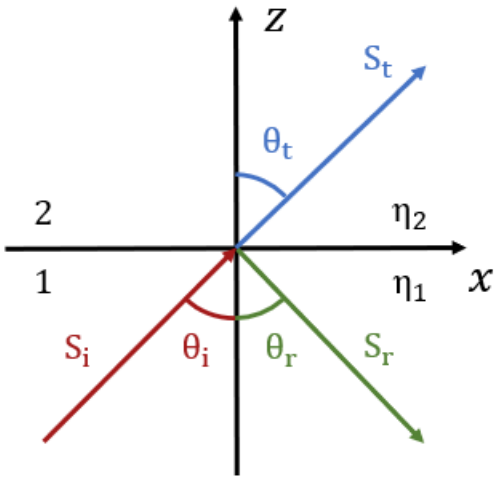

Figure 1: Incident, reflected and transmitted waves.

Due to the interface between two different homogeneous media, a reflected S_r and refracted S_t wave will appear whose angles θ_r and θ_t follow the well-known Snell formula:

$$\frac{\sin\theta_i}{\upsilon_1} = \frac{\sin\theta_r}{\upsilon_1} = \frac{\sin\theta_r}{\upsilon_2} \qquad \frac{\sin\theta_i}{\sin\theta_t} = \frac{\upsilon_1}{\upsilon_2} = \sqrt{\frac{\mu_2\varepsilon_2}{\mu_1\varepsilon_1}} = \frac{\eta_2}{\eta_1} \tag{1}$$

From this formula is clear that when the second medium is denser than the first one ($\eta_2 > \eta_1$), the $\sin\theta_t$ is always real so there is always refraction. In case when ($\eta_1 > \eta_2$) and so the first medium is denser than the second one, the transmission angle θ_t is greater than the incident angle θ_i and there could be total reflection. In this case there is no ray that is refracted in the second medium and an evanescent wave appears at the interface between the two media.

The total reflection phenomenon occurs when there is no real solution for the Snell Law and this occurs when:

$$\theta_i > \theta_{crit} = \arcsin\left(\frac{\eta_2}{\eta_1}\right) \tag{2}$$

The Snell law is a powerful tool in the design of lenses since, by changing the refractive index of a material, it is possible to tilt the angle of the rays and to change the direction of propagation as preferred. As a consequence it is possible to control the direction of propagation of the waves transmitted by a lens antenna in order to have very directive beams.

2.2 FRESNEL FORMULAE

As discussed in previous section, the angle θ is directly related to the refractive index $\eta = \sqrt{\varepsilon_r \mu_r}$. Another important aspect when designing lens antennas is the characteristic impedance ζ of a material defined as:

$$\zeta = \sqrt{\frac{\mu}{\varepsilon}} = \sqrt{\frac{\mu_0 \mu_r}{\varepsilon_0 \varepsilon_r}} = \zeta_0 \frac{\mu_r}{\varepsilon_r} \quad \text{with } \zeta_0 = 376.73\ \Omega \ \text{(in vacuum)} \tag{3}$$

Indeed, the characteristic impedance and the impedance mismatch between two materials define how much of the incident electric field is transmitted and reflected back. This is well defined by the Fresnel formulae for reflection and transmission:

Incident	**Reflected**	**Transmitted**
$E_x^{(i)} = -A_\parallel \cos\theta_i e^{-ir_i}$	$E_x^{(r)} = -\Gamma_\parallel \cos\theta_r e^{-ir_r}$	$E_x^{(t)} = -T_\parallel \cos\theta_t e^{-ir_t}$
$E_y^{(i)} = A_\perp e^{-ir_i}$	$E_y^{(r)} = \Gamma_\perp e^{-ir_r}$	$E_y^{(t)} = T_\perp e^{-ir_t}$
$E_z^{(i)} = A_\parallel \sin\theta_i e^{-ir_i}$	$E_z^{(r)} = \Gamma_\parallel \sin\theta_r e^{-ir_r}$	$E_z^{(t)} = T_\parallel \sin\theta_t e^{-ir_t}$

(4)

Where the parallel and orthogonal reflection and transmission coefficients are expressed in the following way:

Transmission Coefficients

$$T_{\parallel} = \frac{2\zeta_1 \cos\theta_i}{\zeta_2 \cos\theta_i + \zeta_1 \cos\theta_t} A_{\parallel}$$

$$T_{\perp} = \frac{2\zeta_1 \cos\theta_i}{\zeta_1 \cos\theta_i + \zeta_2 \cos\theta_t} A_{\perp}$$

Reflection Coefficients

$$\Gamma_{\parallel} = \frac{\zeta_2 \cos\theta_i - \zeta_1 \cos\theta_t}{\zeta_2 \cos\theta_i + \zeta_1 \cos\theta_t} A_{\parallel}$$

$$\Gamma_{\perp} = \frac{\zeta_1 \cos\theta_i - \zeta_2 \cos\theta_t}{\zeta_1 \cos\theta_i + \zeta_2 \cos\theta_t} A_{\perp}$$

(5)

As shown in the reflection coefficient formulas when $\theta_i = \theta_t = 0^{\circ}$, in order to reduce ideally the reflections to zero, the characteristic impedance of the two media must be equal so that no impedance mismatch is allowed between two different media at the interface. In the case of a lens antenna with a background material as vacuum, the condition of zero reflection is achieved if at the interface between the two media the condition $\zeta = \zeta_0$ is satisfied.

2.3 BASIC PRINCIPLE OF LENSES AND HOMOGENOUS LENSES

When used as receptor, a lens antenna is able to focus the field coming from a given direction into a single point (receptor). On the contrary, when exploited in transmission, lens antennas are able to radiate the energy emitted from a single point (emitter) into a given direction.

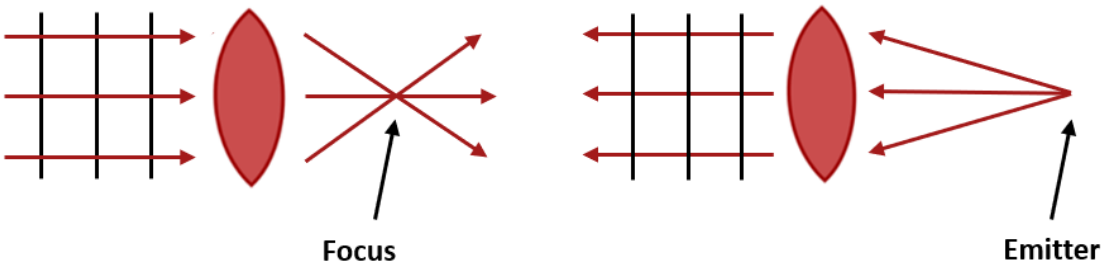

(a) (b)

Figure 2: Lens antenna exploited in reception (a) and transmission (b).

The first basic lens antennas are the homogenous spherical lenses depicted in Figures 2 (a)-(b). They are defined homogenous since they are made of just one uniform dielectric material with non-magnetic properties ($\eta = \sqrt{\varepsilon_r} \neq 1$).

Some problems may be caused by the using of homogenous lenses.

First, aberrations are generated due to the fact that homogenous lenses have just one focal point. If these kind of lenses are employed to scan in a wide angular range by adjusting the feeding position along the focal point plane, aberrations and phase errors appear as in reflector antennas and thus resulting in a decrease of directivity and increase of side lobe levels.

Another issue related to the use of homogenous lenses is reflections. Indeed, since the refractive index of the lens $\eta \neq 1$ at the rim of the lens, the result is that $\zeta \neq \zeta_0$ and so, due to the formulas (3) and (5), reflections occur and the antenna can become very inefficient. A solution for both aberrations and reflections is exploiting graded index lenses [10] and their geodesic implementation.

2.4 GRADED INDEX LENSES

As previously analyzed, homogenous lenses suffer from aberrations and reflections since they have just one focal point and they are made of just one uniform material. One possible way to overcome these inherent limitations is to use graded index lenses [10]. As the name suggests, they are a particular kind of lenses made not of a material with a uniform refractive index η but they are made of a material with a refractive index $\eta(r)$ that is dependent on the radial coordinate r. By implementing a varying spatially refractive index material distribution, the transition between the material of the lens and the vacuum is smoothed in order to achieve at the lens rim, before propagating in free space, $\eta = \sqrt{\varepsilon_r} = 1$ so that reflections are dramatically reduced. Aberrations and phase errors are also solved by graded index lenses, since most of them have rotationally symmetrical properties. Indeed, they are not characterized any more by one single focal point but a focal circle or a section of it. As a consequence, one single feeding can be adjusted in the focal circle or multiport

lenses can be implemented in order to produce multibeam radiation pattern over a wide scanning angular range without ideally any scan losses.

2.4.1 LUNEBURG LENS

Luneburg lens antenna is one kind of the farfield focusing lens antenna. These type of antennas, among them also Ruze lens [6] and Rotman lenses [7], are mainly used to collimate the rays in one single direction in order to achieve high gain and directivity. A figure showing the collimating property of the Luneburg lens in terms of rays along with the 2D distribution of the refractive index is reported below:

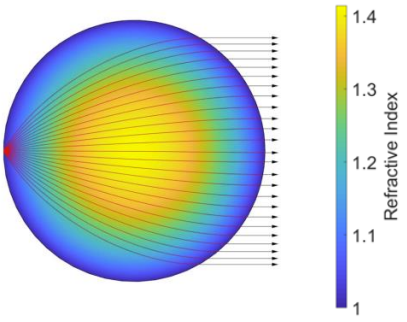

Figure 3: Propagation of rays in a Luneburg lens antenna [11].

$$\eta(r) = \sqrt{2 - (r)^2} \tag{6}$$

Since both Ruze lens and Rotman lenses provide a very limited number of focal points where these lenses can be fed, beam scanning is performed on a reduced scanning range due to phase errors and aberrations. On the contrary, Luneburg lens has no aberrations due to completely rotationally symmetric response with ideally zero scan losses. This results in a wide angular range for beam scanning with a focal circle where to place the feeding and an image point in the farfield where the lens is collimating its rays.

A visualization of this is reported in the figure below:

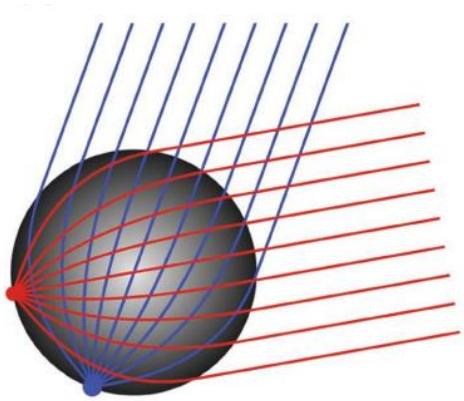

Figure 4: Beam scanning in terms of rays in a Luneburg lens [12].

Reflections can also be solved by exploiting the Luneburg lens solution. Indeed, the spatial distribution of the refractive index guarantees at the rim of the lens $\eta = 1$, and thanks to (3), $\zeta = \zeta_0$. Regarding the implementation of the Luneburg lens, it can be manufactured in three different ways:

1. Discretization of $\eta(r)$ by means of several layers with uniform η;
2. Implementation of metasurfaces in order to vary the effective refractive index $\eta_{eff}(r)$ [13];
3. Exploitation of the geodesic theory;

However some problems arise with the first solution. Indeed, by discretizing the refractive index, layers with uniform refractive index are implemented so that reflections occur. Moreover losses in the dielectric are not negligible when working at higher frequency.

To overcome dielectric losses in mmWave band, several solutions have been proposed in the past such as the use of Substrate Integrated Waveguide (SIW) technology [14].

As a consequence, in high frequency band fully metallic structures are preferred thanks to in vacuum propagation and negligible dielectric losses. The second and third solution previously mentioned rely on this principle.

Here the third principle that is the geodesic principle is explained in detail since it is the method adopted for designing the nearfield lens implemented and simulated in the following sections.

2.5 SINGLE LAYER GEODESIC LENSES

2.5.1 MOTIVATION

As previously mentioned, the limiting problem related to graded index lenses is to rely on lenses that being dielectric suffer from losses when working at higher frequency. One solution was proposed by Rinehart [15]. The idea behind the following mathematical formulation is to replace a 2D single layer model made of dielectric (with graded index properties) with a 3D fully metallic single layer model where propagation occurs inside a cavity between two curved surfaces following the geodesics. The height between the two surfaces parallel plate waveguide (PPW) is chosen less than 0.25λ such that only the transverse electromagnetic mode (TEM mode) can propagate in the cavity.

The analogy can be made only if the two lenses have the same optical path due to the Fermat principle. As a consequence, since the propagation in the geodesics occurs in vacuum and in order to fulfill an equivalence in terms of optical path, the third dimension (the height) is introduced in order to increase the physical length and to mimic, by means of a 3D metallic structure, the spatial distribution $\eta(\mathrm{r})$ of the 2D graded index lens.

Figure 5 shows the relationship between the physical length and optical path of rays. Indeed in the geodesic curve case (solid blue line), the physical length is different with respect to the graded index one (red solid line) but the optical path for the two lenses is the same.

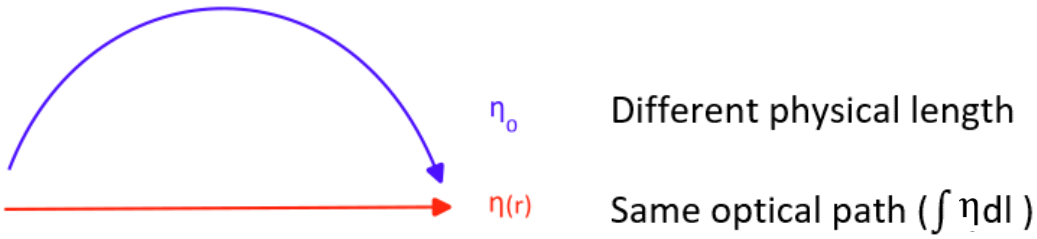

Figure 5: Relationship between physical length and optical path (graded $\eta(r)$ and uniform $\eta_0 = 1$).

2.5.2 ANALYTICAL DERIVATION

Consider a polar coordinate system (r, φ) in a reference plane and a lens with normalized radius equal to 1 centered in the reference plane origin.

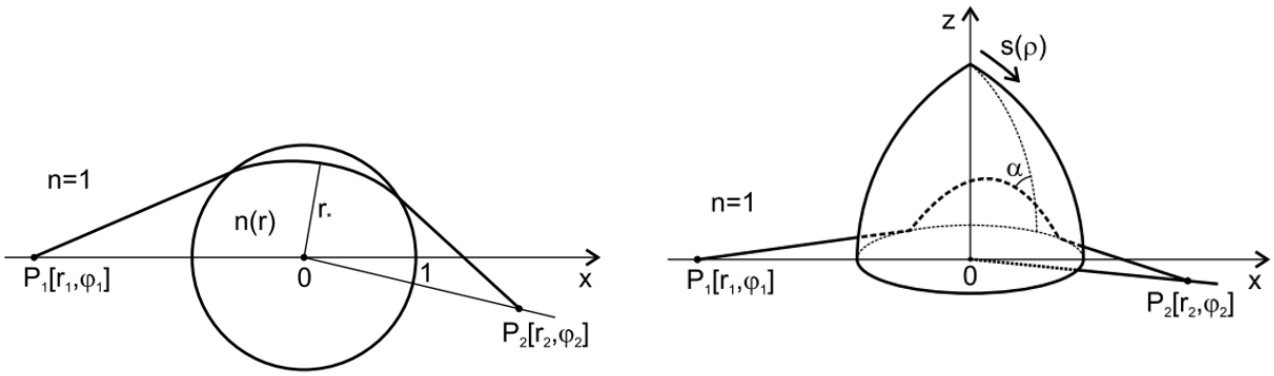

(a) (b)

Figure 6: Graded index lens [16] (a) and geodesic lens [16] (b).

The refractive index of the lens is a graded refractive index only dependent on the normalized radial coordinate r. Moreover the graded refractive index fulfills the condition $\eta(1) = 1$. The background material is considered as vacuum with $\eta = 1$. As shown in Figure 6 (a), all the rays are produced by a point source placed in $P_1[r_1, \varphi_1]$, passing through the lens, and focus at a point $P_2[r_2, \varphi_2]$.

In the geodesic coordinate system $s(\rho)$ is considered, that is the length of the surface computed along the meridian from the z axis to the coordinate of the point along the curve. Two other coordinates are used to describe the point that are the angle θ and the radial coordinate ρ. The analogy between the inhomogeneous 2D graded index lens and geodesic lens is based on imposing the equality between the two optical paths. In the two cases the square of the optical path $d\sigma$ can be written as:

$$\text{Graded index lens: } d\sigma^2 = \eta^2(dr^2 + r^2 d\varphi^2) \tag{7}$$

$$\text{Geodesic lens: } d\sigma^2 = ds^2 + \rho^2 d\theta^2 \tag{8}$$

By assuming the equality for the two coordinate systems $\theta = \varphi$ and between the two formulas (7) and (8), a couple of equations describing the correspondence between the inhomogeneous graded index lens and homogenous geodesic surface are obtained:

$$\begin{cases} \rho = \eta r \\ ds = \eta dr \end{cases} \tag{9}$$

The coordinate ρ is considered to have a maximum at $r = 1$.
By exploiting formulas (9) and by defining the angular momentum L (10) and the ray trajectory (11), the expression (12) is obtained:

$$L = \rho \sin\alpha \tag{10}$$

$$d\theta = \pm \frac{Ls'(\rho)d\rho}{\rho\sqrt{\rho^2 - L^2}} \tag{11}$$

$$\int_L^1 \frac{Ls'(\rho)d\rho}{\rho\sqrt{\rho^2 - L^2}} = \frac{1}{2}\left(M\pi + \arcsin\frac{L}{r_1} + \arcsin\frac{L}{r_2} - 2\arcsin L\right) \tag{12}$$

With $s'(\rho) = \frac{ds(\rho)}{d\rho}$, α the elevation angle, and M real positive number.

The (12) is an Abel integral equation where the unknown is the first derivative $s'(\rho)$ that can be solved to find the geodesic shape corresponding to a certain refractive index spatial distribution.Here is reported the solution of this general equation that is the well-known formula for computing the length on a geodesic surface given the coordinates of the point source $P_1[r_1, \varphi_1]$ and of the image point $P_2[r_2, \varphi_2]$:

$$\begin{aligned} s(\rho) = -\frac{1}{\pi}\Bigg[& \rho \arcsin\sqrt{\frac{1-\rho^2}{{r_1}^2 - \rho^2}} + \rho \arcsin\sqrt{\frac{1-\rho^2}{{r_2}^2 - \rho^2}} \\ & + r_1 \arcsin\left(\rho\sqrt{\frac{{r_1}^2 - 1}{{r_1}^2 - \rho^2}}\right) + r_2 \arcsin\left(\rho\sqrt{\frac{{r_2}^2 - 1}{{r_2}^2 - \rho^2}}\right) \\ & - \sqrt{{r_1}^2 - 1}\arcsin\rho - \sqrt{{r_2}^2 - 1}\arcsin\rho - \arcsin\frac{1}{r_1}\arcsin\rho \\ & - \arcsin\frac{1}{r_2}\arcsin\rho\Bigg] + (M-1)\arcsin\rho + \rho \end{aligned} \tag{13}$$

Thanks to the relation between the height $z(\rho)$ and the length $s(\rho)$ that is $dz^2 = ds^2 - d\rho^2$, the differential equation to derive $z(\rho)$ is obtained from the expression of $s(\rho)$ and is equal to:

$$\frac{dz}{d\rho} = \sqrt{\left(\frac{ds(\rho)}{d\rho}\right)^2 - 1} \tag{14}$$

Depending on the point source and image point and thus on the graded index profile of the lens, the height of the geodesic surface is obtained accordingly.

A plot showing the comparison between a Luneburg lens geodesic curve (Section 2.4.1) and nearfield lens geodesic curves (where the source point is at $r_1 = 1$ and the image point $r_2 < +\infty$) is reported below:

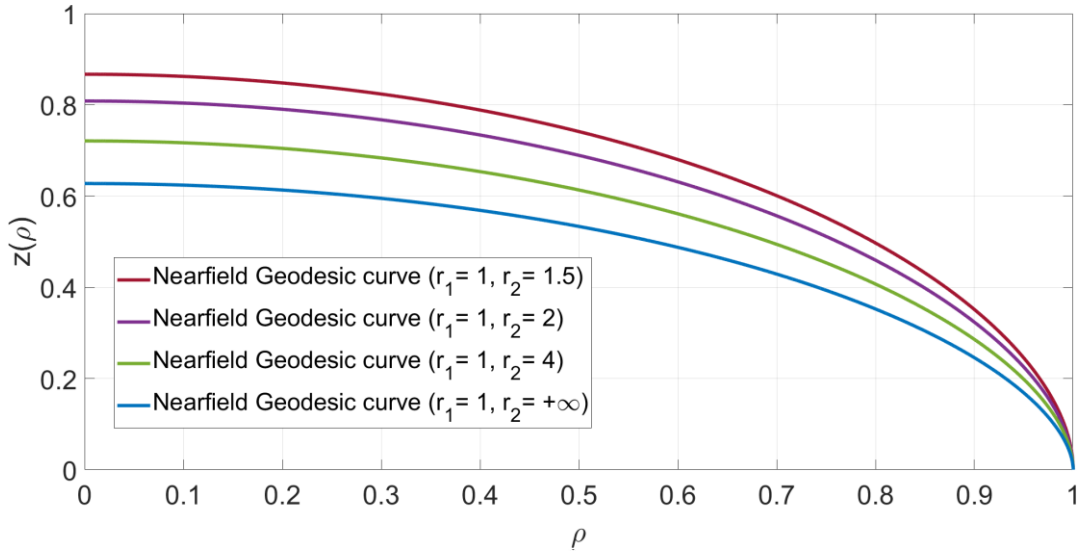

Figure 7: Geodesic height $z(\rho)$ vs ρ in Luneburg and nearfield lenses.

From this plot it's evident that when the image point is placed farther from the lens, the equivalent geodesic height is reduced meaning a lower optical path for the rays to be propagated inside the vacuum cavity of the lens.

Figure 8 shows a 3D vacuum cavity CAD model, obtained by sweeping the geodesic curve along the z axis, of a single-feed nearfield geodesic lens with $r_1 = 1$, $r_2 = 2$:

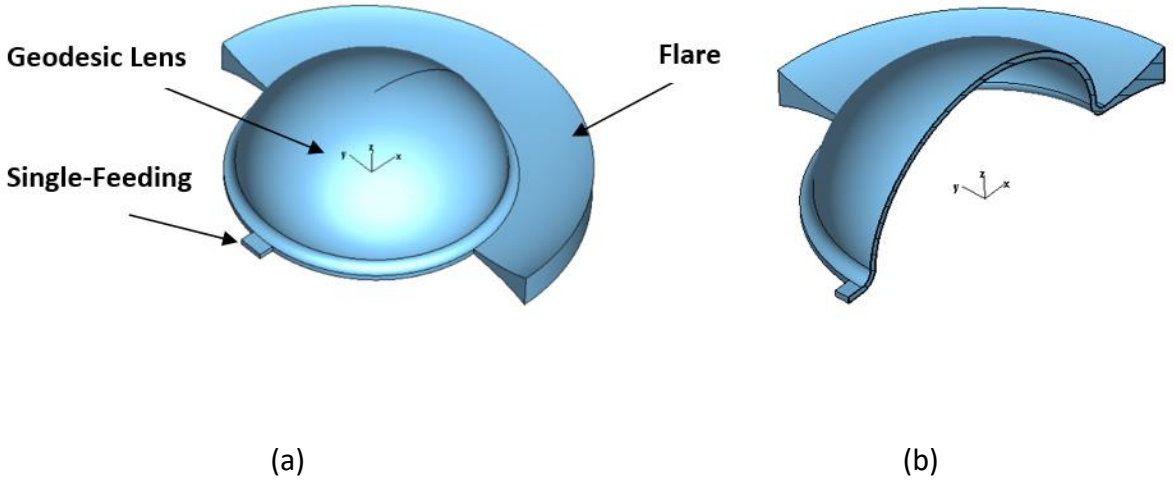

Figure 8: 3D vacuum model of a single-feed nearfield geodesic lens antenna ($r_1 = 1$, $r_2 = 2$) (a) and cross section view (b).

The benefits of the geodesic approach are:

- Wideband;
- Wide angular scanning range with reduced scan losses (thanks to the lens rotationally symmetric property);
- Low ohmic losses that enhance their use in the mmWave band where instead losses in dielectric become a limitation.

2.6 DOUBLE LAYER GEODESIC LENSES

2.6.1 MOTIVATION

A double layer lens antenna is an antenna made of two layers partially connected by a mirror, where generally the two layers (that are parallel plates waveguides defined here upper and lower) are characterized by two different gradient refractive index. The two layers are generally also merged in two different background materials.

The main difference with respect to a single layer one, as the name suggests, is that a double layer lens embeds one more layer (indicated as lower layer) connected to the upper layer (that is the only layer in the single layer case and the beamforming layer in the double layer case) by means of a mirror partially covering the rim of the lens. The gradient refractive indexes of the two layers are referred as $\eta_1(\mathrm{r})$ and $\eta_2(\mathrm{r})$ whereas the two background materials are referred as η_a for the upper waveguide and η_b for the lower waveguide.

The study on double layer lenses started from the work of Rotman [17] that designed what is referred in his work as “Pillbox antenna“ where the two layers are connected by means of a conducting back-wall at the edge of the lens. Due to its rotational symmetric property, this solution provides wider scanning range with respect to parabolic reflector antennas that suffer from aberrations.

This pillbox antenna has been combined with the standard Luneburg lens in order to design a pillbox antenna with ideally no aberrations. This solution is referred in the work [11] as reflective Luneburg lens. In this section a generalization of [11] has been reported with a reference to the work made in [18] and [19].

The double layer solution has been employed along the years due to the compact footprint achieved and the wider angular range scanning capability. Indeed, the feeding is placed in a different layer (the upper one) with respect to the radiating one (the lower one).
This enables to reduce the size of the lens since the beamforming network and the radiating aperture are comprised in the whole volume of the antenna thus

not adding extra space such as in the single layer case [9]. This is fundamental for integration in modern space communication applications.

Moreover, the separation between the two layers (a beamforming layer and radiating layer) adds a further degree of freedom by allowing to extend the radiating section by exploiting its entire area for 2D beam scanning.
Indeed, as in the work [18], a further radiating aperture can be placed such that to produce beam scanning in elevation with high gain. So, the fundamental difference between a single layer and double layer is that all the 2D footprint of the bottom layer could be exploited for radiation whereas in the case of single layer only the 1D rim is exploited for radiation. This of course adds a further degree of freedom in the design of the lens.

2.6.2 ANALYTICAL DERIVATION

In this section a particular lens case is reported [19] whose upper layer is characterized by a gradient refractive index distribution referred as $\eta(r)$ (with a background media with index η_a) and a lower waveguide is filled with the same homogenous material of the background (whose refractive index has been referred as η_b). Moreover, foci at different positions are considered, since for the case of study of this Master Thesis a nearfield lens is considered. Regarding the working principle, the incident rays coming from the source point $P_s\ [r_s, \varphi_s]$ in a background material with homogenous refractive index η_a, propagate inside the upper waveguide with a gradient refractive index $\eta(r)$, before impinging on a mirror at the lens rim and then being reflected in the lower waveguide with homogenous refractive index η_b and focused in an image point $P_i\ [r_i, \varphi_i]$ (Figure 9 (a)). Next the geodesic derivation is also considered (Figure 9 (b)).

Figures 9 (a)-(b) show how the refractive index $\eta(r)$ in a double layer gradient index lens is mimicked by means of a modulation of the normalized height of the lens $z(\rho)$.

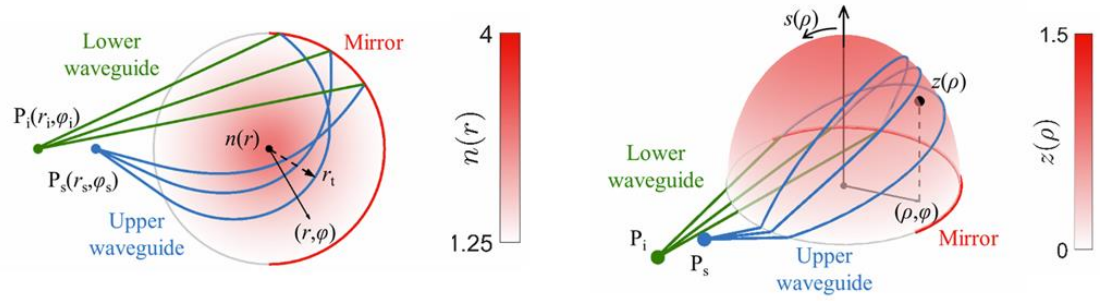

(a) (b)

Figure 9: Double layer gradient refractive index lens in a polar coordinate system (r, φ) (a) [19] and its geodesic equivalence in a cylindrical coordinate system (ρ, φ, z) (b) [19].

Starting from Figure 9 (a), the angle swept from the ray during the propagation between two points at radii r_1 and r_2 can be computed as:

$$\Delta\varphi = \pm \int_{r_1}^{r_2} \frac{r^{-1} L dr}{\sqrt{\eta^2(r) r^2 - L^2}} \tag{15}$$

The change of sign in the integral happens after the turning point of the ray referred as r_t. For the whole trajectory from the source point $P_s\,[r_s, \varphi_s]$ to the image point $P_i\,[r_i, \varphi_i]$, the angle swept $\Delta\phi = \varphi_i - \varphi_s$ satisfies the following equation:

$$\int_{r_t}^{1} \frac{r^{-1} L dr}{\sqrt{\eta^2(r) r^2 - L^2}} = \frac{1}{2}\left[\Delta\phi - \int_{1}^{r_s} \frac{r^{-1} L dr}{\sqrt{{\eta_a}^2(r) r^2 - L^2}} - \int_{1}^{r_i} \frac{r^{-1} L dr}{\sqrt{{\eta_b}^2(r) r^2 - L^2}} - 2\int_{\frac{L}{\eta_b}}^{1} \frac{r^{-1} L dr}{\sqrt{{\eta_b}^2(r) r^2 - L^2}}\right] \equiv g(L) \tag{16}$$

Where $g(L)$ corresponds to half the angle swept inside the upper layer with gradient refractive index distribution $\eta(r)$. The first two integrals on the right refer to the propagation out of the lens (in the background material of the upper layer η_a and in the background material of the lower layer η_b) whereas the last term is the propagation in the bottom layer. By solving the integrals, an expression for $g(L)$ is found:

$$g(L) = \frac{1}{2}\left[\Delta\phi - \pi + \arcsin\frac{L}{\eta_a r_s} + \arcsin\frac{L}{\eta_b r_i} + \arcsin\frac{L}{\eta_b} - \arcsin\frac{L}{\eta_a}\right] \tag{17}$$

Here an analogy can be made between the expression of $g(L)$ for the double layer case (where a mirror is applied) and for the single layer case (without the use of a mirror) as reported in the work [16]. In [16] the expression of $g(L)$ (in the case where $\eta_a = \eta_b = 1$) is the following:

$$g(L) = \frac{1}{2}\left[\Delta\phi + \arcsin\frac{L}{r_s} + \arcsin\frac{L}{r_i} - 2\arcsin\,(L)\right] \tag{18}$$

In the double layer case there is an extra term π and the last term of equation (18) is not present due to the fact that the rays are reverted in the lower layer when impinging on the mirror that is not present in the single layer case. By starting from equation (16), the analytical solution for deriving the geodesic shape (Figure 9 (b)) of the upper layer (corresponding to the gradient index of the same) is reported below. Indeed, by imposing conditions (9) to the integral equation (16), the same equation can be rewritten as:

$$\int_L^R \frac{Ls'(\rho)d\rho}{\rho\sqrt{\rho^2 - L^2}} = g(L) \tag{19}$$

Where $R = \eta_a$ is the maximum radius of the lens. The integral equation (19) can be inverted thus obtaining:

$$s'(\rho) = \frac{-2\rho}{\pi}\frac{\partial}{\partial\rho}\int_{\rho}^{R}\frac{g(L)dL}{\sqrt{L^2-\rho^2}} \tag{20}$$

If equation (17) is placed in equation (20), an expression of the meridian length $s(\rho)$ (computed from the z axis center) is derived:

$$\begin{aligned} s(\rho) = {} & A\rho + \eta_a B \arcsin\frac{\rho}{\eta_a} \\ & -\frac{1}{\pi}\left[\eta_a r_s \arcsin\left(\rho\sqrt{\frac{r_s{}^2-1}{\eta_a{}^2 r_s{}^2-\rho^2}}\right)\right. \\ & + \eta_b r_i \arcsin\left(\frac{\rho}{\eta_a}\sqrt{\frac{\eta_b{}^2 r_i{}^2-\eta_a{}^2}{\eta_b{}^2 r_i{}^2-\rho^2}}\right) + \eta_b \arcsin\left(\frac{\rho}{\eta_a}\sqrt{\frac{\eta_b{}^2-\eta_a{}^2}{\eta_b{}^2-\rho^2}}\right) \\ & \left. -\left(\eta_a\sqrt{r_s{}^2-1} + \sqrt{\eta_b{}^2 r_i{}^2-\eta_a{}^2} + \sqrt{\eta_b{}^2-\eta_a{}^2}\right)\arcsin\frac{\rho}{\eta_a}\right] \end{aligned} \tag{21}$$

Where $A = \frac{1}{2} - \frac{1}{\pi}\left(\arcsin\sqrt{\frac{\eta_a{}^2-\rho^2}{\eta_a{}^2 r_s{}^2-\rho^2}} + \arcsin\sqrt{\frac{\eta_a{}^2-\rho^2}{\eta_b{}^2 r_i{}^2-\rho^2}} + \arcsin\sqrt{\frac{\eta_a{}^2-\rho^2}{\eta_b{}^2-\rho^2}}\right)$ and $B = M - \frac{1}{2} + \frac{1}{\pi}\left(\arcsin\frac{1}{r_s} + \arcsin\frac{\eta_a}{\eta_b r_i} + \arcsin\frac{\eta_a}{\eta_b}\right)$ with the assumption that $1 \le \eta_a \le \eta_b$, r_s and r_i normalized to the R and $\Delta\phi = (M+1)\pi$.

3 DOUBLE LAYER NEARFIELD GEODESIC LENS ANTENNA

3.1 DESIGN AND METHODOLOGY

Referring to the theory in Section 2.6, a double layer nearfield focusing geodesic lens has been designed and simulated according to the design requirements reported below in Table 1. In particular, the lens consists of two layers (upper and lower) connected by a mirror with $45°$ slope covering partially the rim of the lens. Indeed, the rays coming from the upper layer, after impinging on the mirror, are reflected in the bottom layer where they are focused. Each layer is confined between two metal pieces thus forming a PPW region.

Center Frequency	60 GHz
Bandwidth	56-62 GHz
HPBW	$> 20°$
Roll-off	< 3 dB
Scanning range (H plane)	$\pm 55°$

Table 1: Design requirements.

The double layer nearfield geodesic lens curve of this work is a particular case derived from the general equation (21). Since the purpose of this work is not to design a double layer lens where the two layers are merged in two different media for generating leaky waves as in the works [20][21], the background refractive indexes of the first layer and second layer are chosen equal to the one

of vacuum so that $\eta_a = 1$ and $\eta_b = 1$. Furthermore, following the derivation of section 2.6, the bottom layer refractive index has been set equal to the refractive index of the background material η_b that is vacuum.
The lens is of geodesic type so that it's a fully metallic lens, suitable for high frequency applications.

Referring to the work [9], in order to fulfill the design requirements and to find the theoretical middle curve of the lens profile, the meridian length $s(\rho)$ of the double layer lens has been obtained by setting in equation (21) as source point $r_s = 1$ (normalized to the radius of the lens) and image point $r_i = 2.9$ (so that the lens is focusing in the nearfield).

The radially normalized middle curve profile of the double layer lens is then derived by substituting the obtained $s(\rho)$ in the differential equation (14) and by solving it with a MATLAB script in an iterative way.
Even though no closed form analytical expression can be derived for the normalized lens profile $z(\rho)$, it can be approximated (with an error of an order of magnitude 10^{-3}) with a super ellipse formula that is:

$$z(\rho) = h_0(1 - \rho^p)^{1/q} \tag{22}$$

where h_0 is the normalized height of the lens with respect to the radius R whereas both p and q are lens parameters that define its shape.

The optimal approximation curve has been obtained in terms of $h_0 = 1.415$, $p = 2.069$ and $q = 2.051$.

A comparison between the lens profile, obtained by deriving the meridian length from equation (21) and then substituting $s(\rho)$ in equation (14), and its super ellipse approximation, expressed by equation (22), is reported below.
As shown in Figure 10, low approximation error has been found by approximating the lens profile (14) with equation (22) by substituting as h_0, p and q the values previously reported. In the following sections, the super ellipse formula has been employed due to its simpler form for optimization purposes.

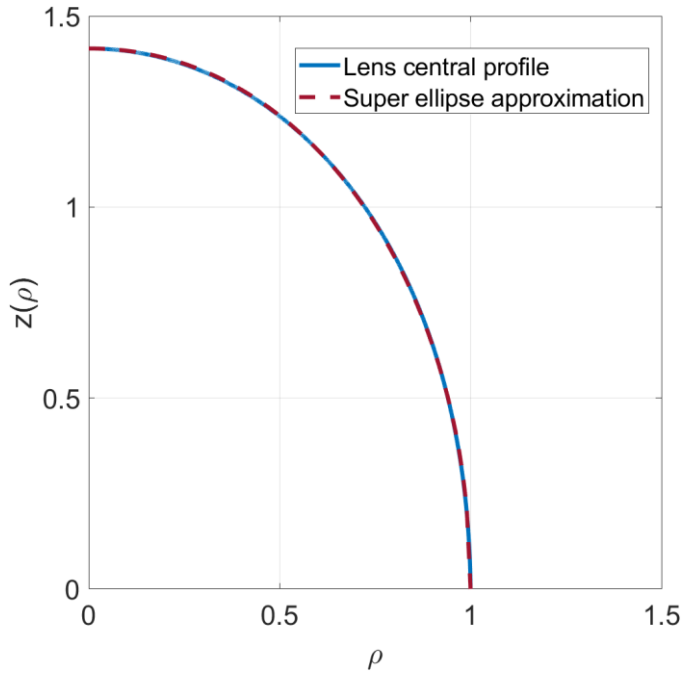

Figure 10: Comparison between lens profile derived from differential equation (14) and approximation curve based on super ellipse formulation.

As a consequence, the implemented nearfield geodesic double layer lens is fed at the rim of top layer that is $r_s = 1$ and focus all the rays, emerging from the mirror, at a radial coordinate $r_i = 2.9$ in the bottom layer.

3.2 DESIGN PARAMETERS

Regarding the design parameters, the radius of the lens has been set equal to $R = 4\lambda = 20\ \text{mm}$ ($\lambda = 5\ \text{mm at } 60\ \text{GHz}$) whereas the height of the middle profile of the lens is equal to $h = 5.6\lambda = 28.3\ \text{mm}$. The PPW thickness is equal to $0.16\lambda = 0.8\ \text{mm}$ that is less than 0.25λ at the maximum frequency of the band so that only the TEM mode can propagate inside the lens. This PPW thickness has been already chosen in another work [22] due to manufacturing easiness in the frequency band of interest ($56 - 62\ \text{GHz}$).
Belonging to the nearfield family lenses, the total height of this nearfield geodesic double layer lens is higher with respect to the Luneburg geodesic double layer lens due to the longer optical path needed.

The lens shape plot showing both the central profile and the inner and outer profiles (including also the thickness of the PPW) is reported in Figure 11. In addition to the lens profile, the mirror connecting the upper layer and bottom layer is reported in the same plot as well as the chamfer feeding.

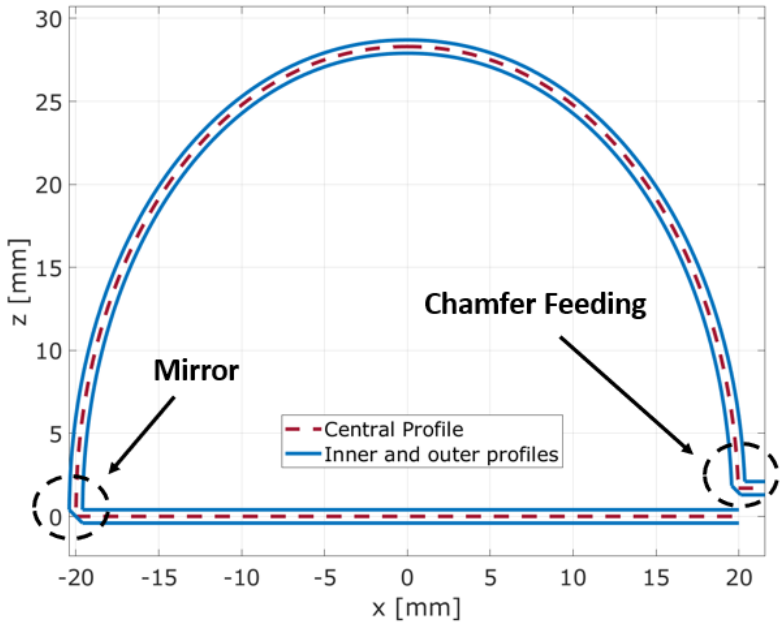

Figure 11: Central and inner and outer profiles with PPW region of the nearfield double layer geodesic lens. The mirror and chamfer feeding are also included in the plot.

3.3 MIRROR

A mirror is needed in order to reflect the rays impinging from the first layer to the bottom layer of the lens antenna, thus adding a π extra phase shift. With no mirror, no transition would be possible between the upper layer and bottom layer thus reflecting back all the rays coming from the beamforming layer. It is a 45° slope mirror , partially covering the rim of the radiating layer of the lens antenna, with equal length and height. A simplified model has been implemented in CST by considering just the mirroring part of the double layer lens. As a result, this model is not considering the radial curvature of the lens antenna due to application of perfect magnetic conductor (PMC) boundary

conditions along the y axis thus saving computational heaviness. In order to reduce the reflection coefficient S_{11} below $-15\,\mathrm{dB}$ in the frequency band of interest $56-62\,\mathrm{GHz}$, an optimization of the mirror has been performed in CST. Figure 12 shows the mirror design (b) and simulated frequency behavior of the S_{11} parameter (a).

As highlighted in Figure 12, an S_{11} lower than $-15\,\mathrm{dB}$ has been obtained between $56-62\,\mathrm{GHz}$ choosing a length and height of the mirror equal to $0.16\lambda = 0.8\,\mathrm{mm}$.

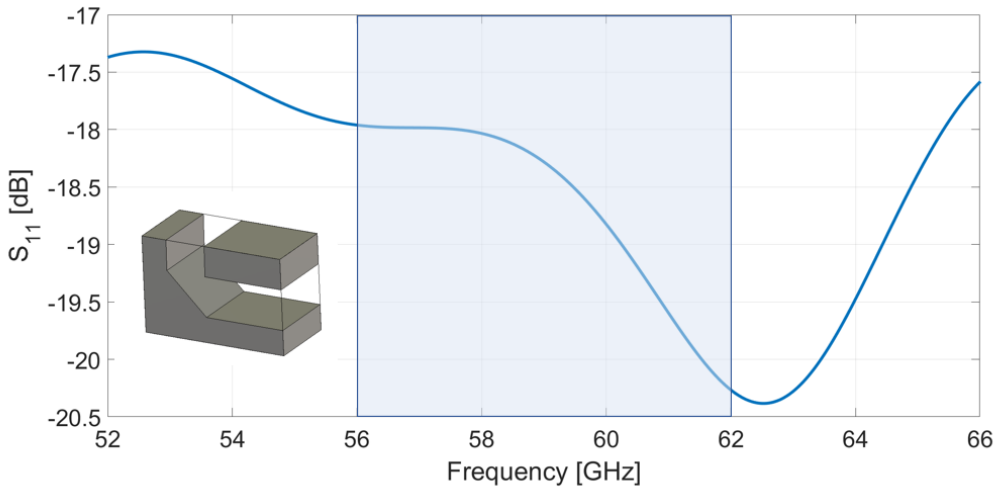

(a)

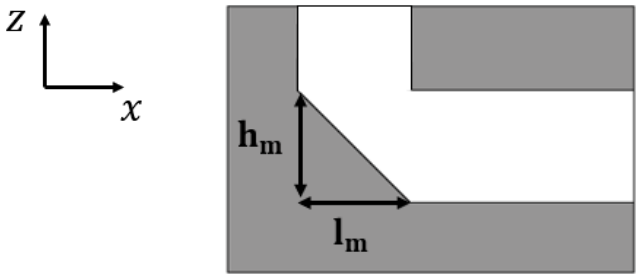

(b)

Figure 12: Reflection coefficient of the mirror (a). The mirror has an height $h_m = 0.8\,\mathrm{mm}$ and a length $l_m = 0.8\,\mathrm{mm}$ (b).

3.4 FLARE

An exponential flare is needed in order to match the impedance of the TEM mode of the lens antenna with free space. Without the flare, the antenna would radiate as a waveguide with height equal to PPW thickness that is $0.8\ \mathrm{mm}$. This would lead to strong reflection and high value of reflection coefficient S_{11} due to impedance mismatch.

In order to analyze the reflection coefficient at flare section, a simplified model has been designed by considering just the flare part of the lens without considering the whole structure and the radial curvature of the lens. This results in a simplification in terms of computational heaviness.

Figure 13 shows the flare design (b) and how this simplified model has been optimized in order to reduce the S_{11} below $-15\ \mathrm{dB}$ in the frequency band $56 - 62\ \mathrm{GHz}$ (a).

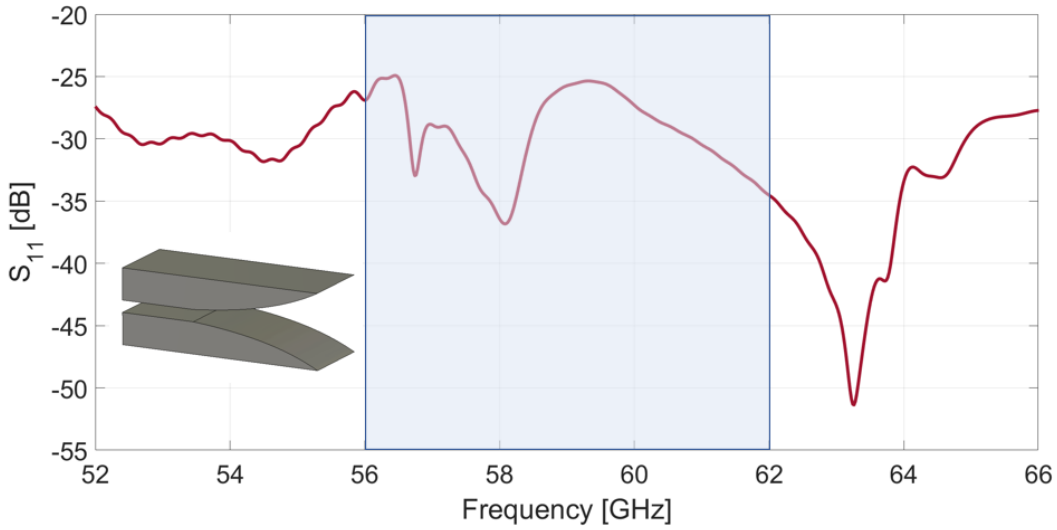

(a)

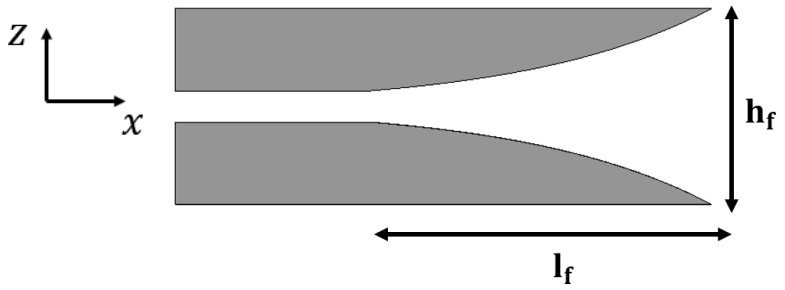

(b)

Figure 13: Reflection coefficient of the flare (a). The flare has an height $h_f = 5\ mm$ and a length $l_f = 8.75\ mm$ (b).

3.5 FEEDING

In order to feed the lens antenna and match the impedance and height of the PPW with the ones of a standard waveguide, a stepped horn with two steps has been implemented. The standard waveguide employed for this design is WR19 ($a = 4.8\ mm, b = 2.39\ mm$) already used in another work [22].
The choice of this kind of waveguide is mainly due to its frequency range since it can work in the frequency band $56 - 62\ GHz$ of interest. The metal and air part of the stepped horn transition along with a cross section view is reported below in Figure 14:

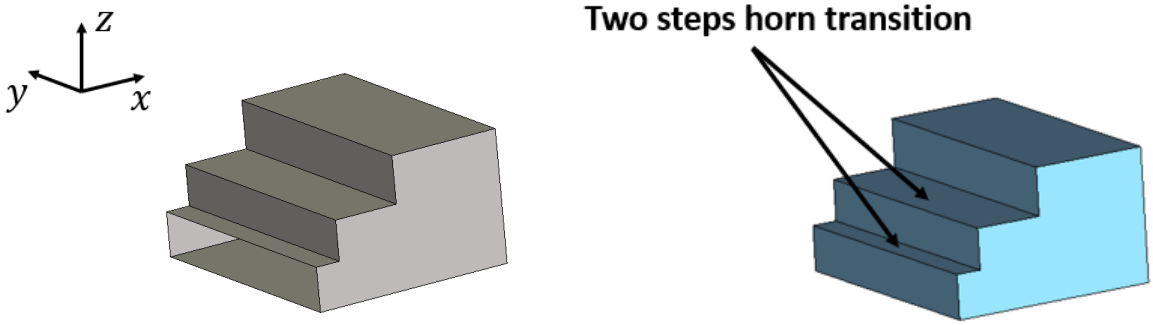

(a) (b)

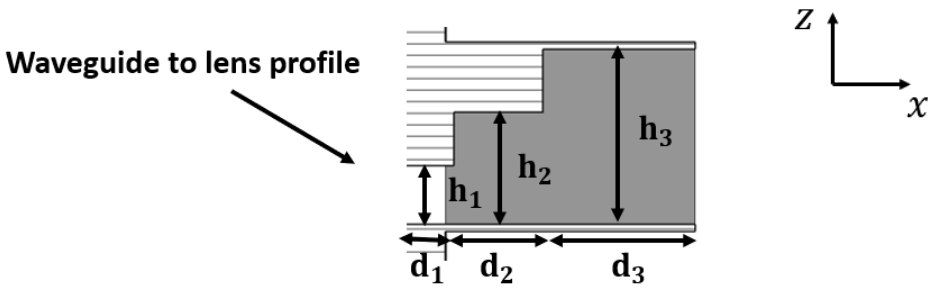

(c)

Figure 14: Metal (a) and air part (b) of stepped horn transition. A cross section view of the metal part is also included with stepped horn parameters (c).

The optimization of the stepped horn parameters have been carried out by designing a simplified model considering just the feeding and part of the lens for computational easiness. Moreover PMC boundary conditions have been considered thus neglecting the radial curvature of the lens and simplifying the model. A figure showing the implemented model has been reported below:

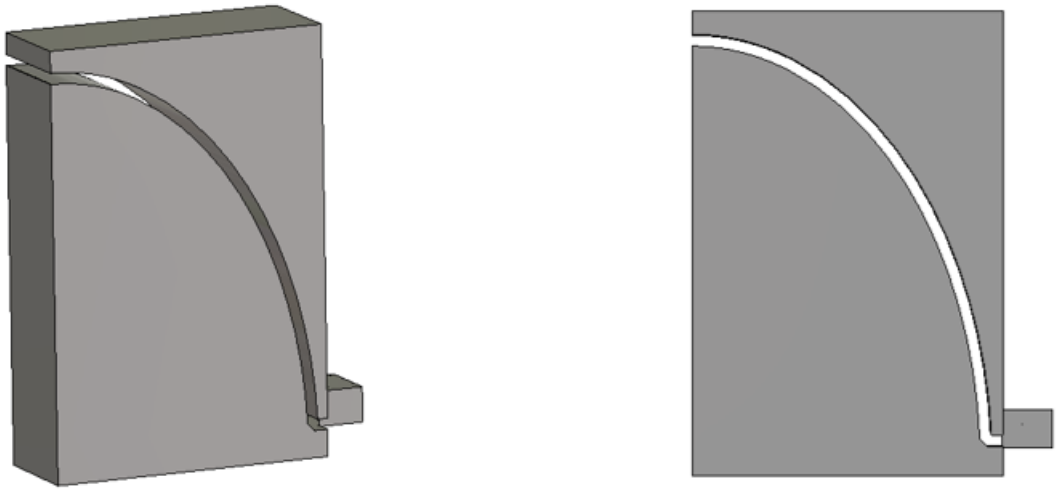

(a) (b)

Figure 15: Simplified model for S_{11} optimization. Perspective (a) and side view (b).

The feeding parameters of the model of Figure 14 (c) have been optimized in CST in order to obtain a reflection coefficient S_{11} below -20 dB in the frequency band $56 - 62$ GHz. The result of this simulation is reported below in Figure 16:

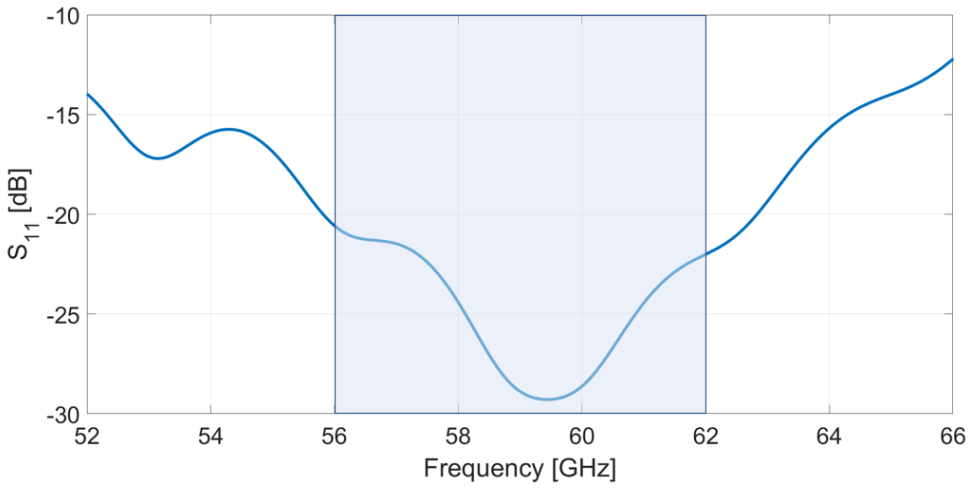

Figure 16: Reflection coefficient S_{11} at transition between stepped horn and lens profile.

Here below are the optimal values found as a result of the previous simulation:

Parameter	Value [mm]
$\mathbf{h_1}$	0.8
$\mathbf{h_2}$	1.53
$\mathbf{h_3}$	2.39
$\mathbf{d_1}$	0.35
$\mathbf{d_2}$	1.22
$\mathbf{d_3}$	2.08

Table 2: Optimal values of stepped horn parameters.

3.6 SINGLE PORT DOUBLE LAYER LENS LAYOUT AND RESULTS

A single port double layer lens based on design parameters shown in previous sections has been designed and simulated in CST. Figures 17 and 18 show the layout of the lens reporting both the air part and the metal part of the lens.

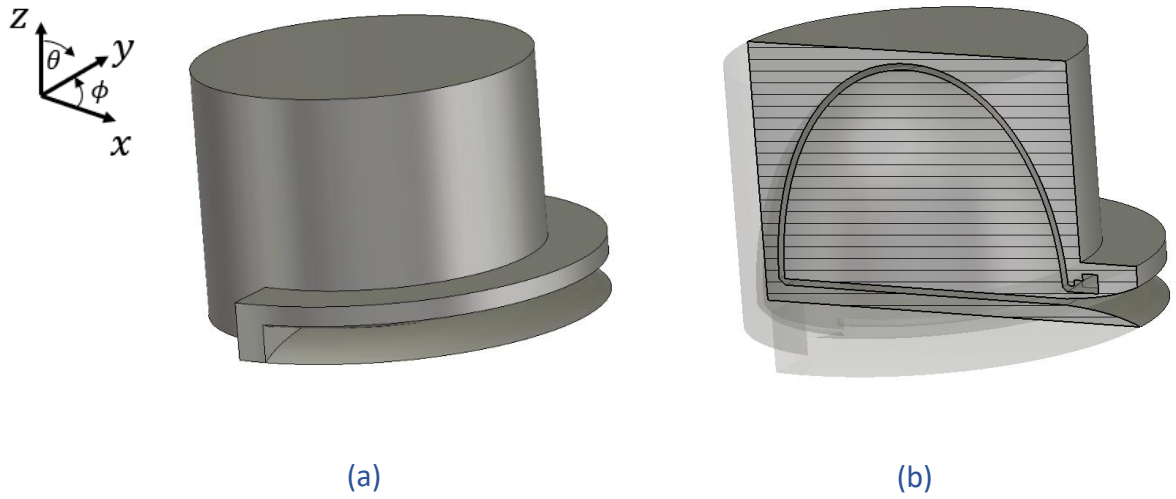

(a) (b)

Figure 17: Perspective view metal part (a) of double layer lens antenna and cross section view (b).

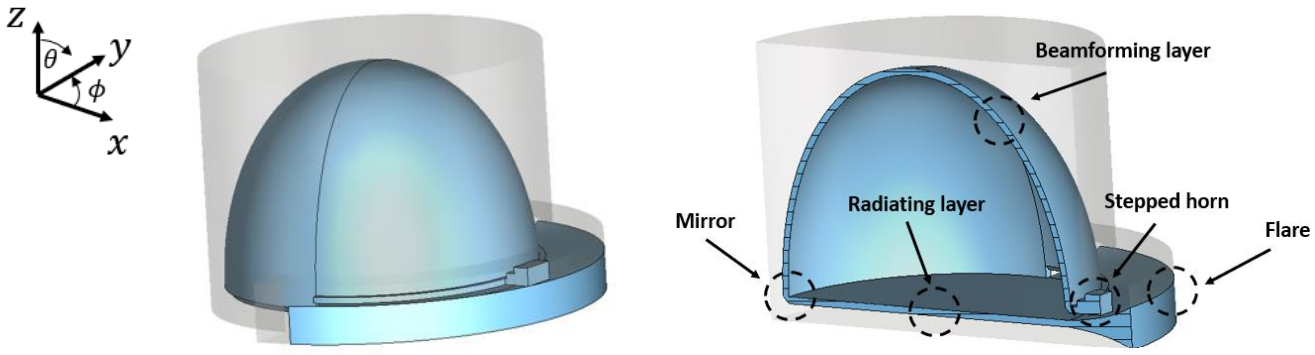

(a) (b)

Figure 18: Perspective view air part (a) of double layer lens antenna and cross section view (b).

All the models previously reported have been implemented without considering the transition from coaxial-to-waveguide needed to excite the fundamental mode TE_{10} of the WR19 rectangular waveguide. The model has been simulated as perfect electric conductor (PEC) with transient mode solver in CST. The patterns at three different frequencies of the band ($\mathrm{f_{min}} = 56\ \mathrm{GHz}, \mathrm{f_c} = 60\ \mathrm{GHz}, \mathrm{f_{max}} = 62\ \mathrm{GHz}$) are obtained and plotted below in Figure 19:

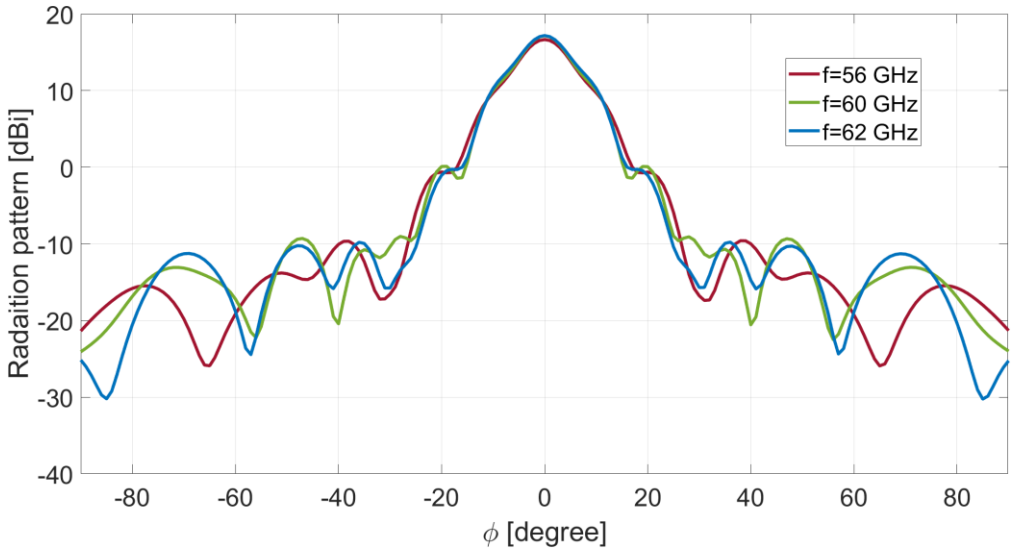

Figure 19: Farfield patterns at $\mathrm{f_{min}} = 56\ \mathrm{GHz}, \mathrm{f_c} = 60\ \mathrm{GHz}, \mathrm{f_{max}} = 62\ \mathrm{GHz}$.

Detailed information about radiation patterns represented in Figure 19 are reported in Table 3 below:

Frequency [GHz]	56	60	62
Directivity [dBi]	16.7	17.1	17.2
HPBW [°]	10.5	10.3	10.5
SLL [dB]	-17.3	-17	-17.4

Table 3: Farfield results at $\mathrm{f_{min}} = 56\ \mathrm{GHz}, \mathrm{f_c} = 60\ \mathrm{GHz}, \mathrm{f_{max}} = 62\ \mathrm{GHz}$.

As can be observed from Table 3, the radiation patterns at the three analyzed frequencies don't satisfy the design requirements of this work in terms of HPBW. Indeed an HPBW $\mathrm{smaller\ than}$ $20°$ does not fulfill the requirements in Table 1 thus resulting in poor performance in terms of beam coverage. If a multiport lens would have been built with this lens profile, an unacceptable roll-off between crossover points would arise thus not allowing to have beam coverage between $\pm 55°$ with a roll-off lower than $3\ \mathrm{dB}$.

This result is due to the fact that the meridian length derived from equation (21) and then the profile of the lens from (14) don't take into account the presence of chamfer feeding of the final design. Indeed, this issue is remarked in Figure 10 where the lens should be fed at $\rho = 1$ and $z = 0$, where the slope of the lens is ∞, leading to an unfeasible solution due to the presence of strong reflections.

Furthermore, in double layer design, the mirror and bottom radiating layer must be considered as well. As a result, a chamfer feeding is inserted in the model thus requiring an optimization of the lens profile in order to achieve the desired performance in terms of HPBW. In Figure 20, a comparison of the reflection coefficient S_{11} computed with full model simulation and considering just the simplified model (already explained in detail in section 3.3) is reported.

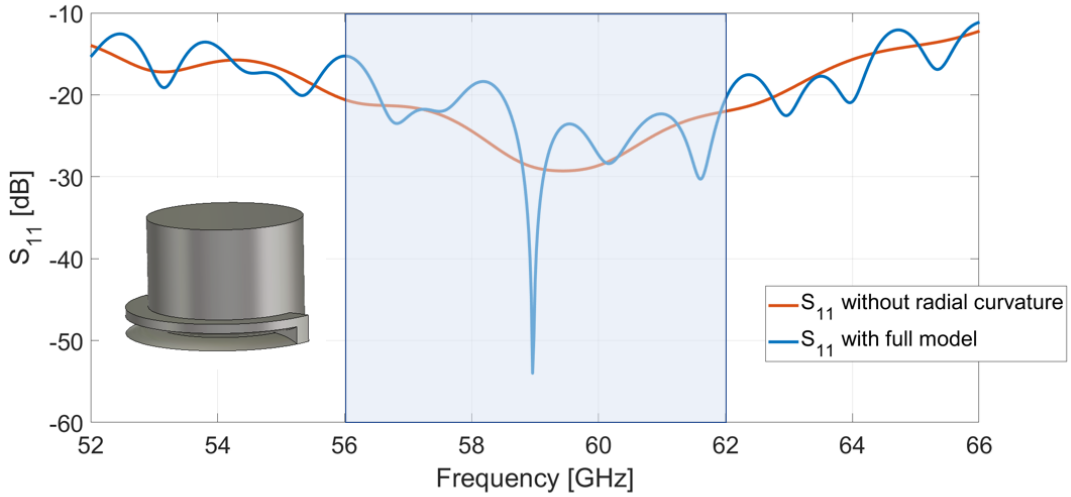

Figure 20: S_{11} reflection coefficient including full model and simplified model of Figure 16.

As depicted, a good agreement has been found between the simplified model simulation (already shown in Figure 16) and the model considering the radial curvature of the lens (full model), thus resulting in a S_{11} lower than -15 dB in $56-62$ GHz band.

3.7 OPTIMIZATION OF DOUBLE LAYER NEARFIELD GEODESIC LENS PROFILE

As mentioned in section 3.3, the profile of the lens must be optimized, due to the fact that the profile parameters previously used (in terms of h_0, p and q) derived from differential equation (14) don't take into account the presence of chamfer feeding. Indeed, chamfering the profile of the lens for feeding purposes, leads to a truncation of the lens profile that cannot be fed at $\rho = 1$ and $z = 0$, as shown in Figure 10, but at $\rho = 1$ and $z = 0.08$ (radially normalized coordinates).

Since part of the optical path of the lens has not been considered due to presence of the chamfer, the height of the final lens profile must be increased in order to preserve the equality in terms of total optical path and have the desired performance in terms of focusing properties and lens behavior.

Indeed, if the optical path is reduced due to removal of part of the lens for feeding insertion, the rays are not focused anymore at the desired focal point in the nearfield region. In order to achieve the desired performance in terms of HPBW, the super ellipse equation describing the profile of the lens has been optimized thus leading to a final profile for a double layer geodesic lens design.

Indeed, the super ellipse equation, approximating the differential equation (14), already implemented in previous simulations, is equal to:

$$z(\rho) = 1.415 \cdot (1 - \rho^{2.069})^{1/2.051} \tag{23}$$

where $h_0 = 1.415$, $p = 2.069$ and $q = 2.051$.

As previously remarked, an optimization in CST has been performed on equation (23). The optimized super ellipse equation found is equal to:

$$z(\rho) = 1.44 \cdot (1 - \rho^{2.008})^{1/2} \tag{24}$$

where $h_0 = 1.44$, $p = 2.008$ and $q = 2$.

A comparison between the two middle curve lens profiles described by equations (23) and (24) is reported below:

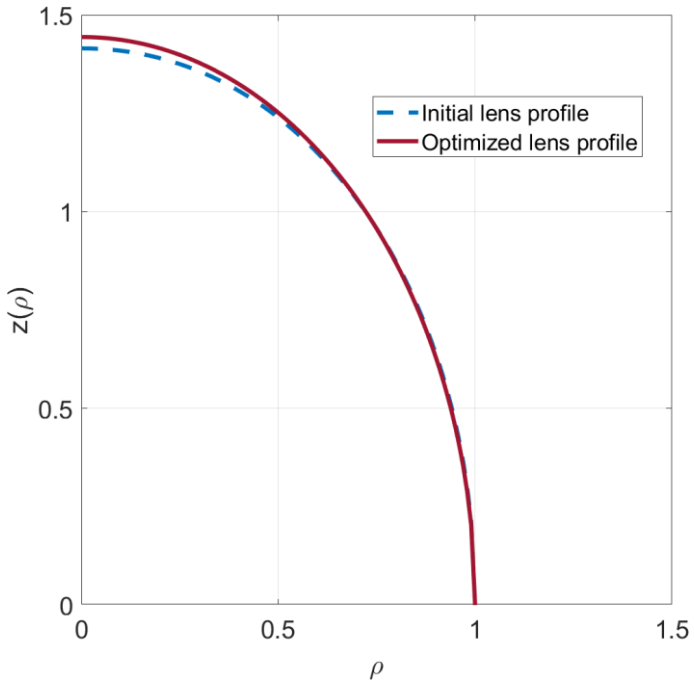

Figure 21: Initial lens profile from (23) and optimized lens profile from (24).

As it is evident from Figure 21, the optimized lens is characterized by an increase of height due to the higher h_0.

A plot showing both the middle profile (ideal profile) and the realized profile (with a PPW thickness equal to $0.8\ mm$) for the optimized lens from equation (24) is reported below:

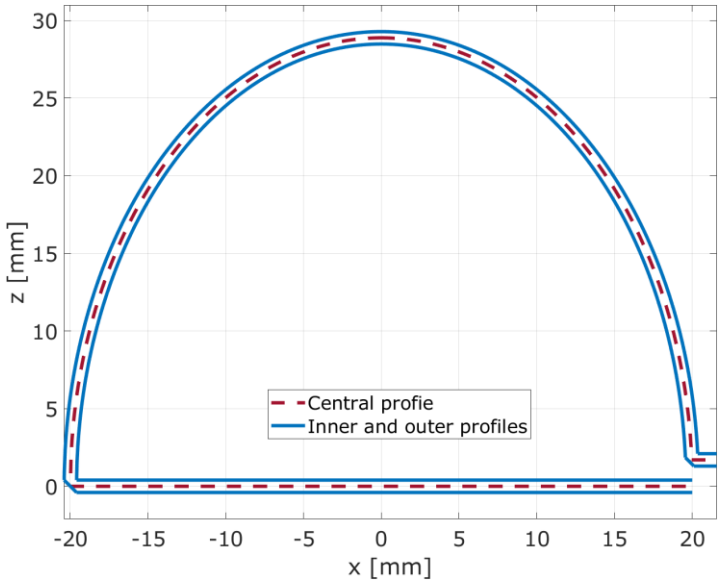

Figure 22: Central and inner and outer profiles with PPW region for both the initial lens design and optimized one. In this plot both the flare and stepped horn are not shown.

3.8 OPTIMIZED SINGLE PORT DOUBLE LAYER LENS LAYOUT AND RESULTS

The optimized lens has been implemented and simulated as perfect electric conductor (PEC) with transient mode solver in CST. The metal and air parts of this lens are the same as the ones already shown in Figure 17 and Figure 18.

The main difference between the two models is the lens shape in terms of height and lens profile (in terms of h_0, p and q). All the design parameters already analyzed for the mirror, flare and feeding are here retained.

Figure 23 shows a comparison of the radiation patterns simulated for the two lens antennas with initial lens profile, described by equation (23), and optimized lens profile described by equation (24).

Both radiation patterns have been simulated at the three frequencies of interest ($f_{min} = 56$ GHz, $f_c = 60$ GHz, $f_{max} = 62$ GHz) thus covering all the possible bandwidth of operation and being represented with respect to the spherical angles in the range $\phi = [-90°, 90°]$ and $\theta = 90°$.

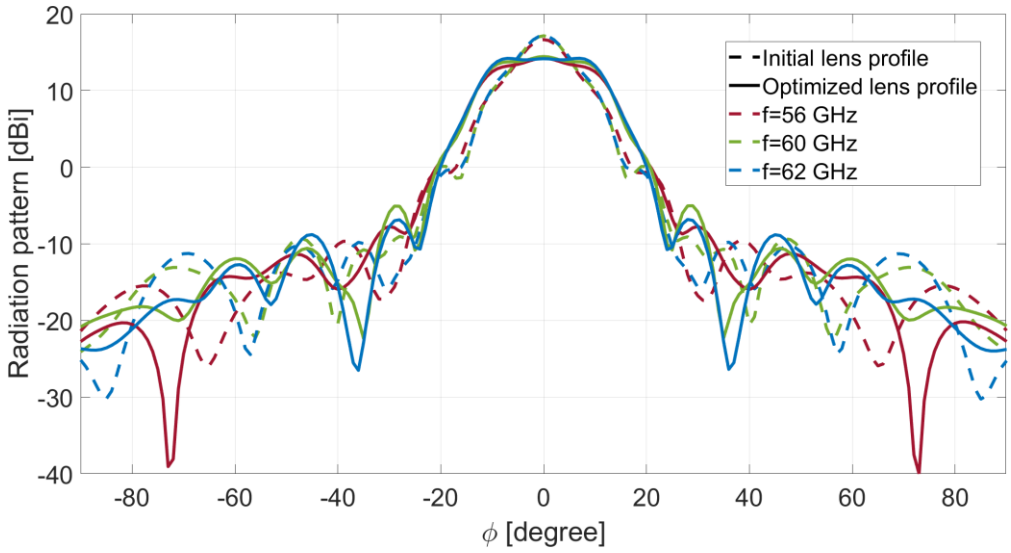

Figure 23: Radiation patterns including the initial lens profile and optimized lens profile.

Detailed analysis of main radiation parameters at the three frequencies of interest have been carried out both for the initial lens profile and optimized lens and the results are reported in Table 4:

	Initial lens Profile			Optimized lens Profile		
Frequency [GHz]	56	60	62	56	60	62
Directivity [dBi]	16.7	17.1	17.2	14.2	14.4	14.2
HPBW[°]	10.5	10.3	10.5	23.6	23.8	24.2
SLL [dB]	-17.3	-17	-17.4	-22	-19.5	-21

Table 4: Farfield results at $f_{min} = 56$ GHz, $f_c = 60$ GHz, $f_{max} = 62$ GHz for both the initial lens profile and optimized lens profile.

As can be observed from Table 4, the design requirements in terms of half-power beam width (HPBW) are fulfilled by the optimized lens profile. Indeed, with respect to the initial design, the HPBW at the three frequencies of interest for the optimized lens is higher than 20° thus allowing to achieve, in a multiport lens, a roll-off lower than $3\ \mathrm{dB}$ between the beams at crossover points in the coverage angle of interest. Moreover, as it is evident from Table 4, an improvement is also obtained in terms of side lobe levels (SLL) (that are lower with respect to the initial design).

However, these improvements in terms of HPBW and SLL of the optimized lens profile are obtained at expense of lower directivity with respect to the initial profile.

This was expected since the goal of our design was to design a lens antenna able to increase the beam coverage with low roll-off between the beams. As a result, a reduction on the gain must be accepted in order to widen the beam and achieve a stable aggregate gain in the farfield.

Below the absolute value of electric field $\vec{\mathrm{E}}$ for the single port optimized profile lens is reported at three different frequencies ($\mathrm{f_{min}} = 56\ \mathrm{GHz}, \mathrm{f_c} = 60\ \mathrm{GHz}, \mathrm{f_{max}} = 62\ \mathrm{GHz}$). Beamforming layer electric field representation in terms of absolute value is reported in Figures 24-25-26 (a). Moreover simulations showing in detail just the radiating layer are reported in Figures 24-25-26 (b) as well.

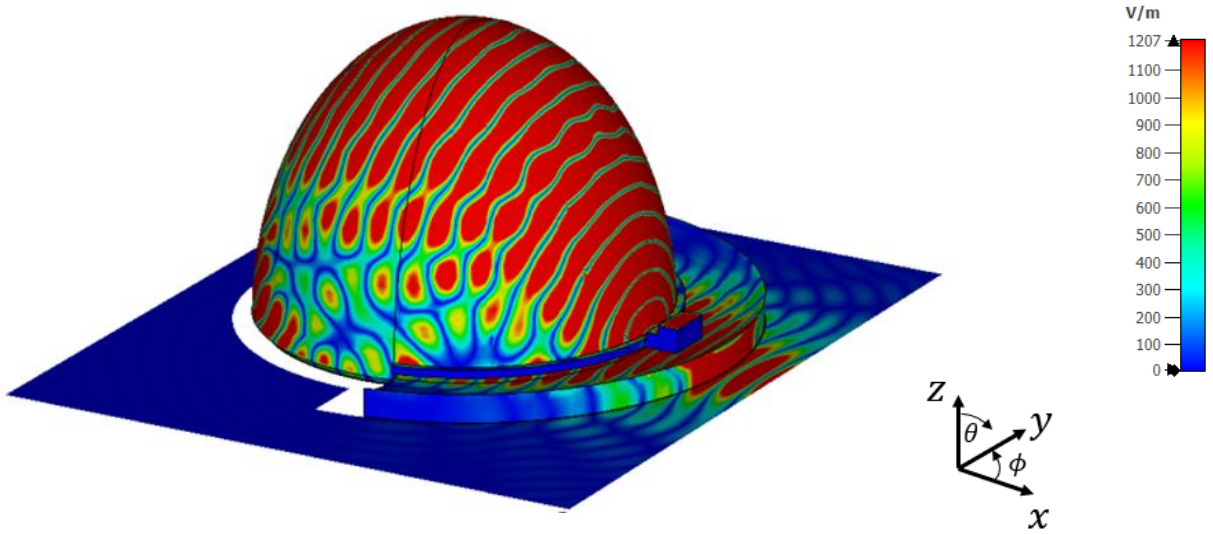

(a)

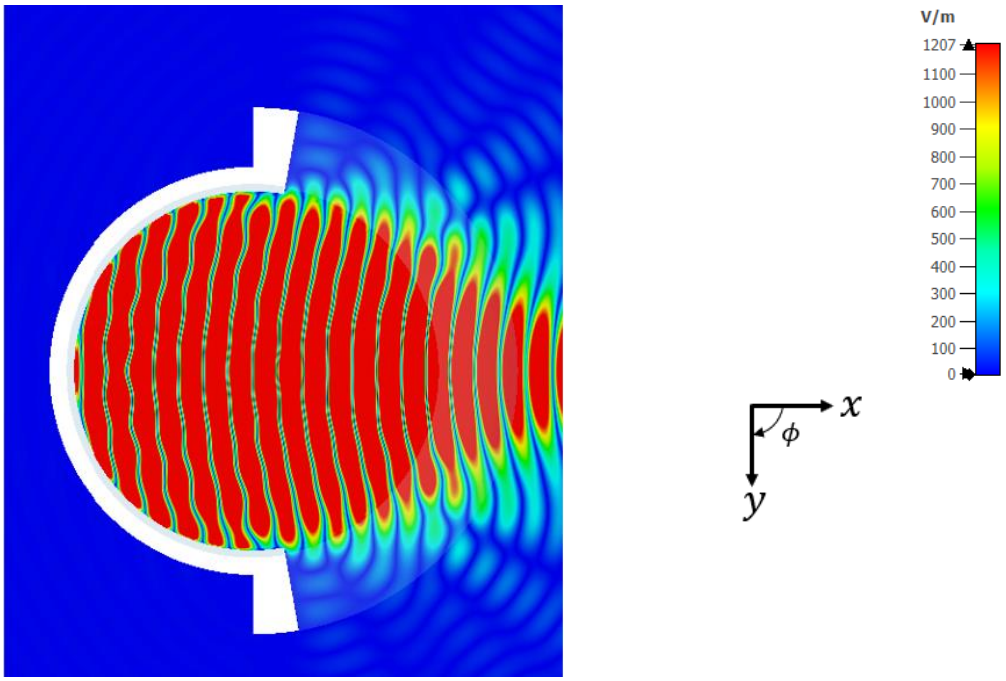

(b)

Figure 24: Absolute value of $\vec{E}$ at 56 GHz. Perspective view (a) and bottom view (b) of the lens model are included.

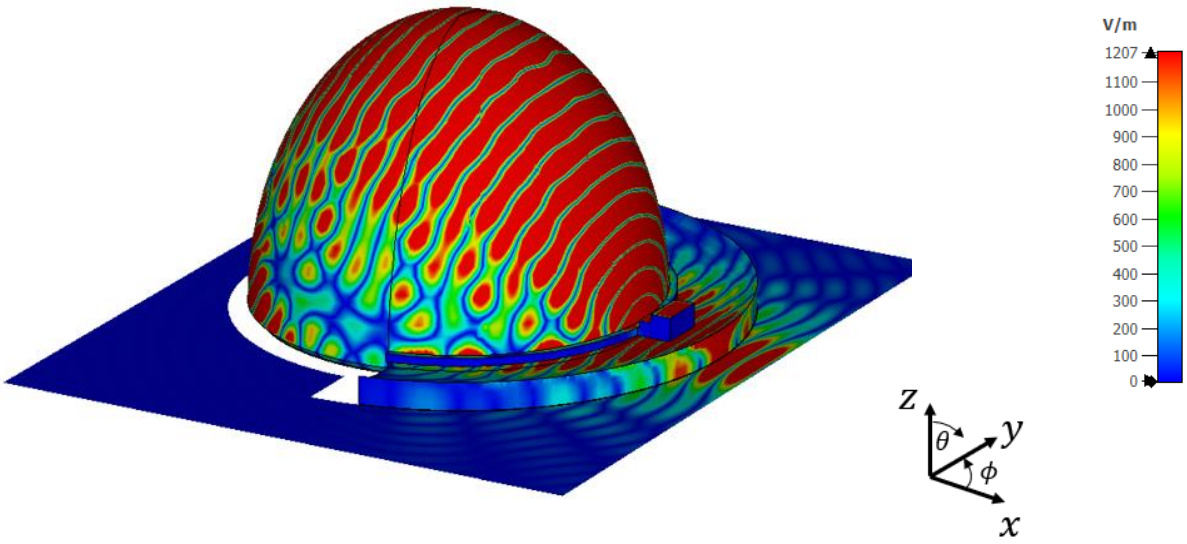

(a)

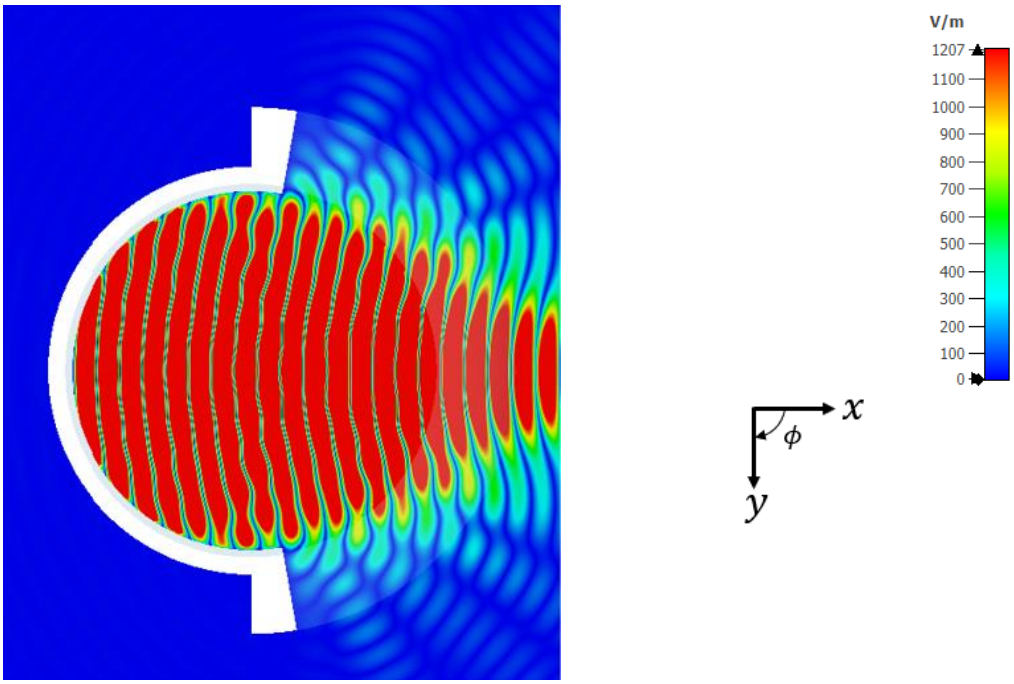

(b)

Figure 25: Absolute value of $\vec{E}$ at 60 GHz. Perspective view (a) and bottom view (b) of the lens model are included.

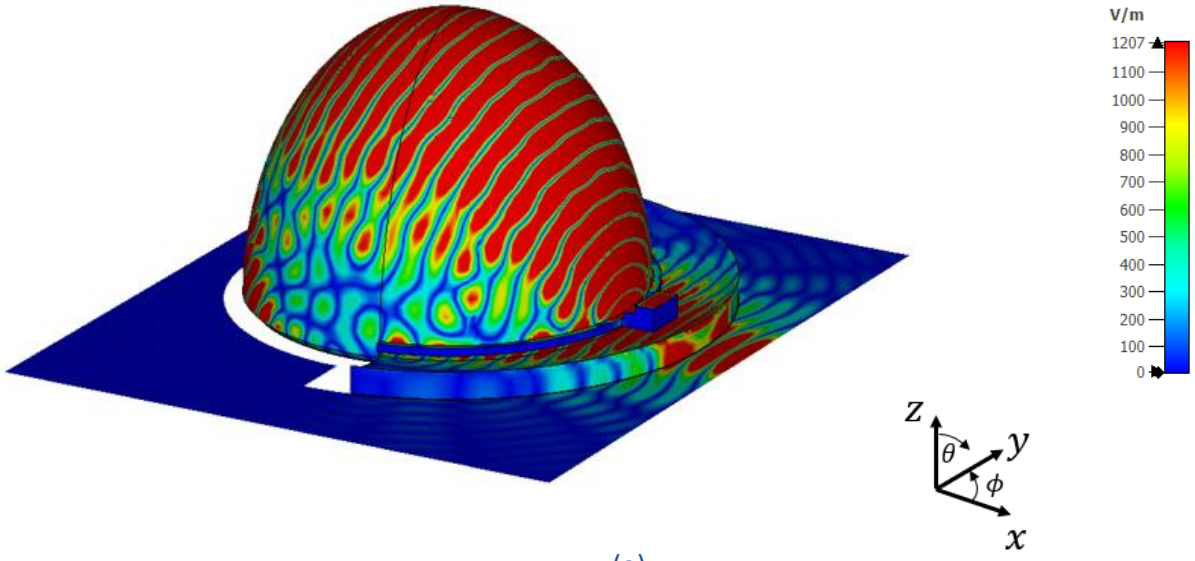

(a)

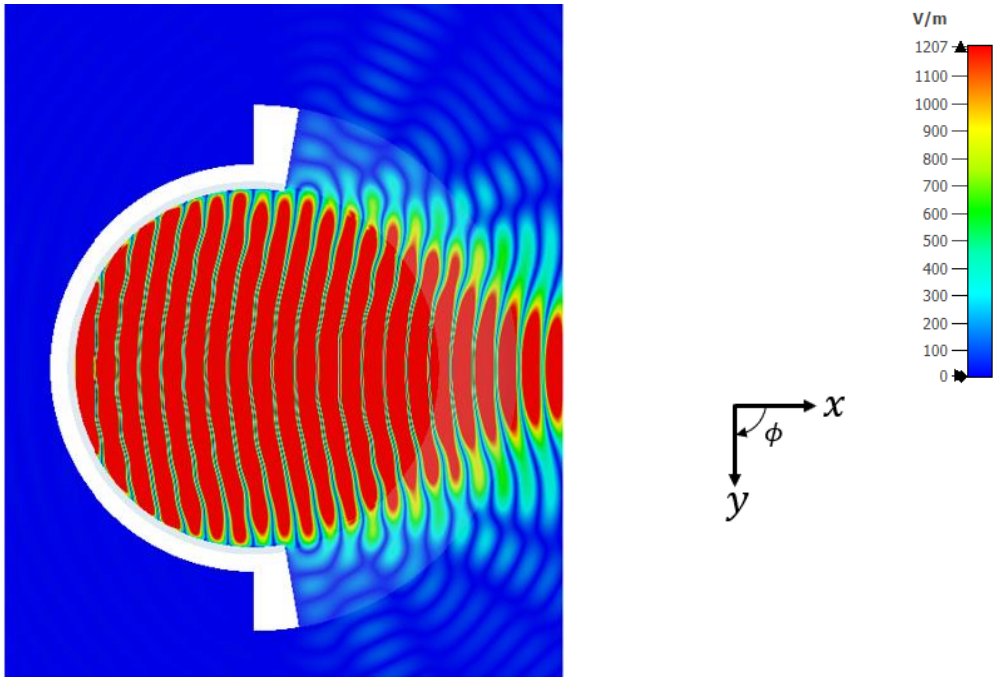

(b)

Figure 26: Absolute value of $\vec{E}$ at 62 GHz. Perspective view (a) and bottom view (b) of the lens model are included.

The phase of the electric field $\vec{E}$ at the three frequencies ($f_{min} = 56$ GHz, $f_c = 60$ GHz, $f_{max} = 62$ GHz) is reported below:

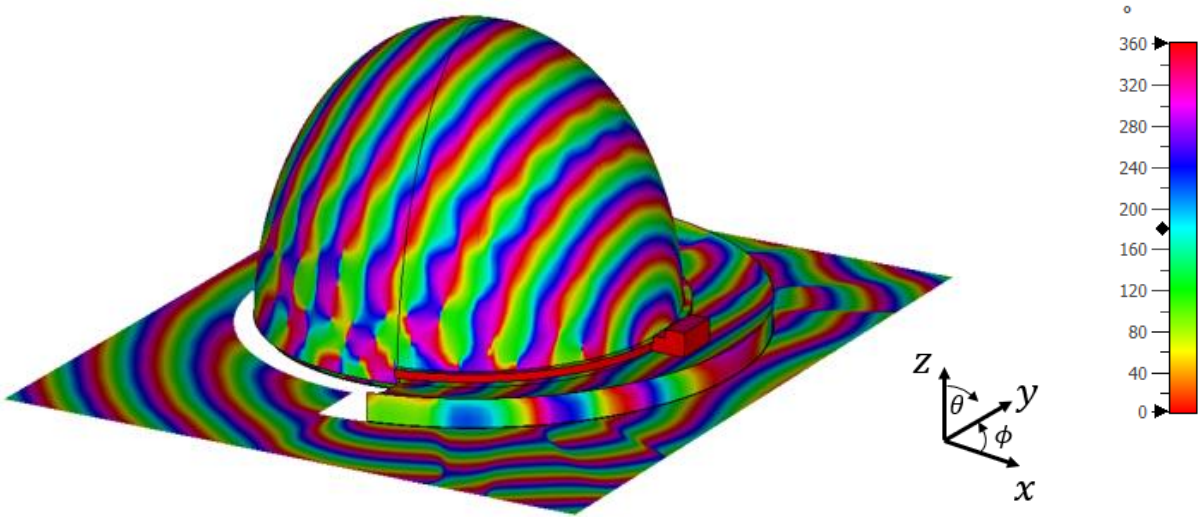

(a)

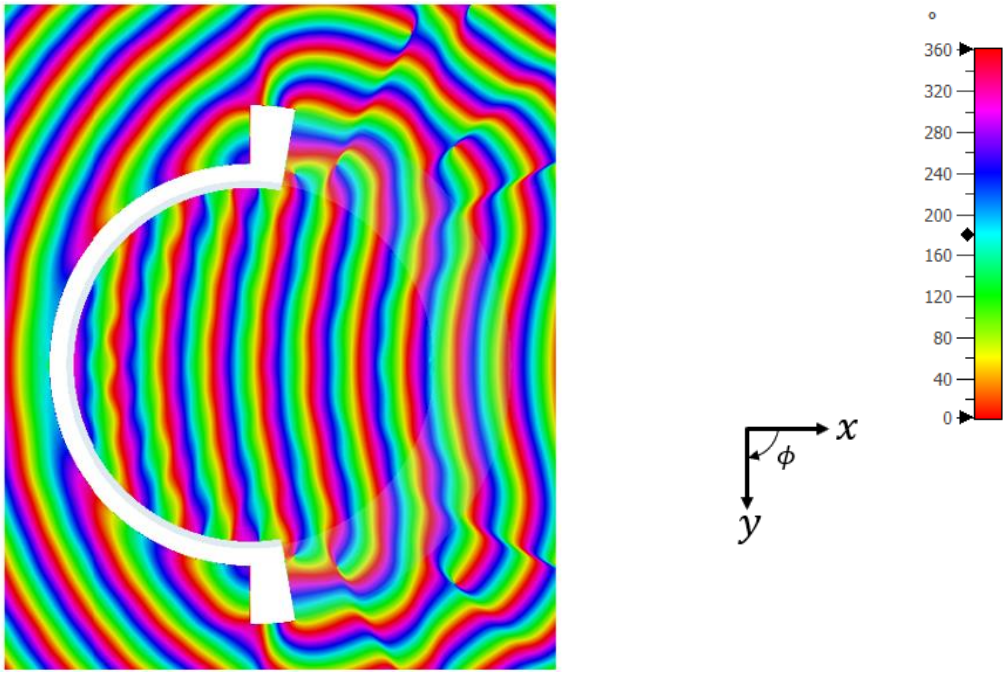

(b)

Figure 27: Phase of $\vec{E}$ at 56 GHz. Perspective view (a) and bottom view (b) of the lens model are included.

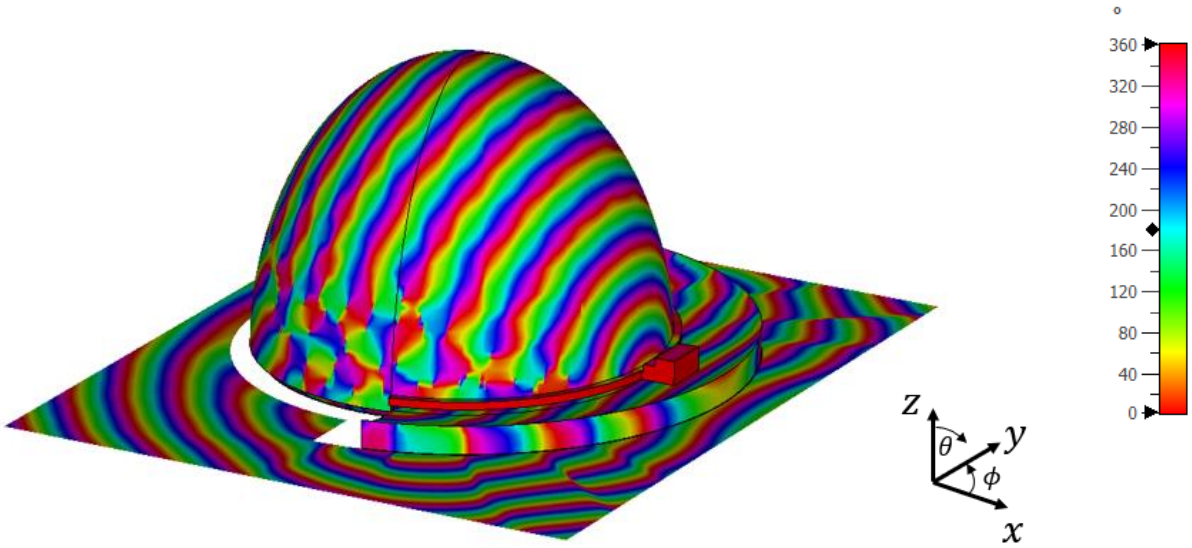

(a)

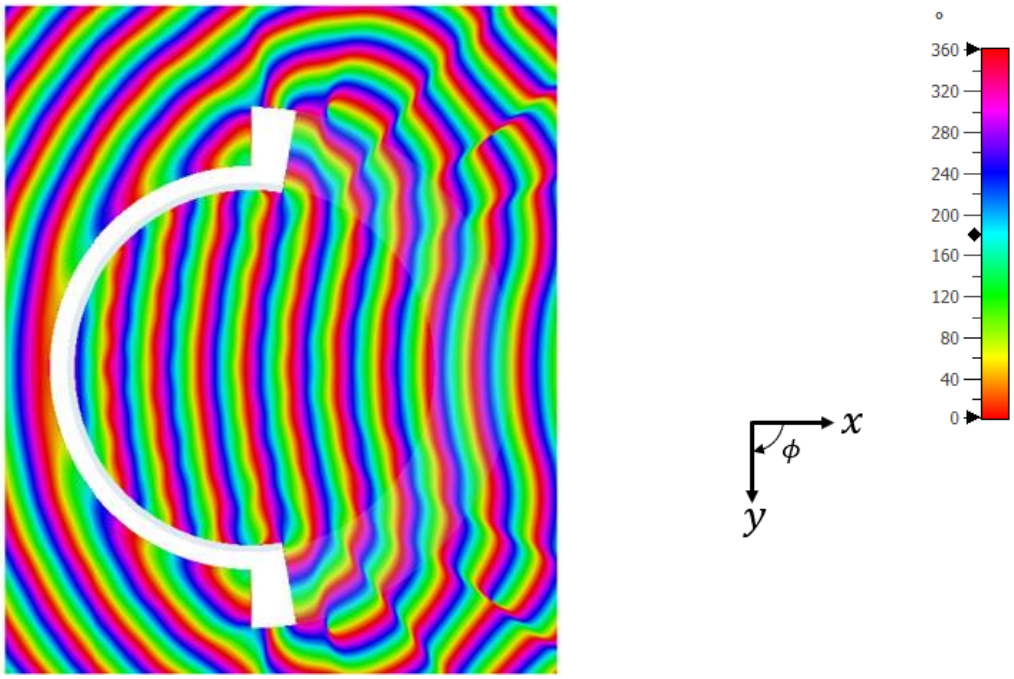

(b)

Figure 28: Phase of $\vec{E}$ at 60 GHz. Perspective view (a) and bottom view (b) of the lens model are included.

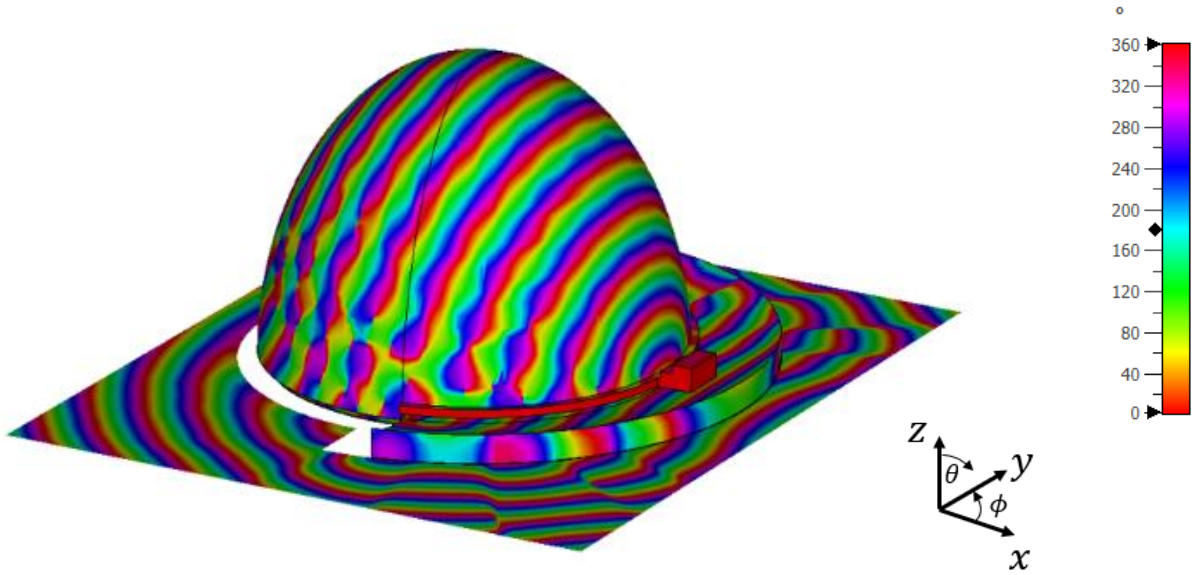

(a)

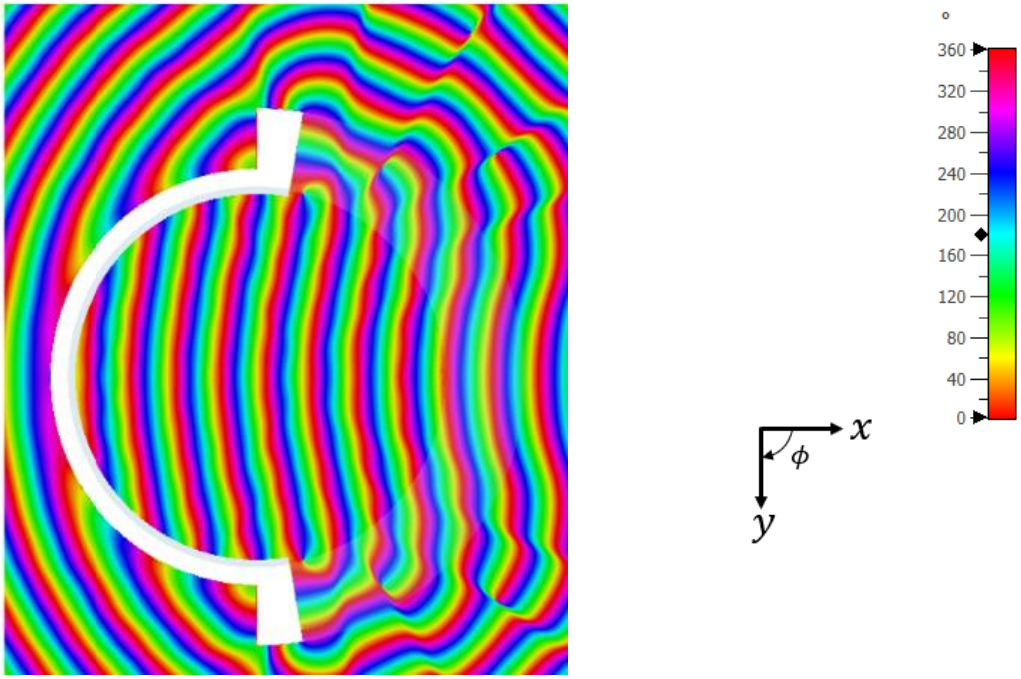

(b)

Figure 29: Phase of $\vec{E}$ at 62 GHz. Perspective view (a) and bottom view (b) of the lens model are included.

As it is shown in absolute value plots, the lens is working as a nearfield focusing lens (in all the frequency band of interest $56 - 62$ GHz) thus focusing all the rays in the nearfield region of the lens. This property enables widening of the radiation pattern main beam. Moreover, in Figure 30 the S_{11} reflection coefficients of both the initial lens profile and the optimized one are compared thus showing the neglecting influence of the optimization of lens profile on the reflection coefficient:

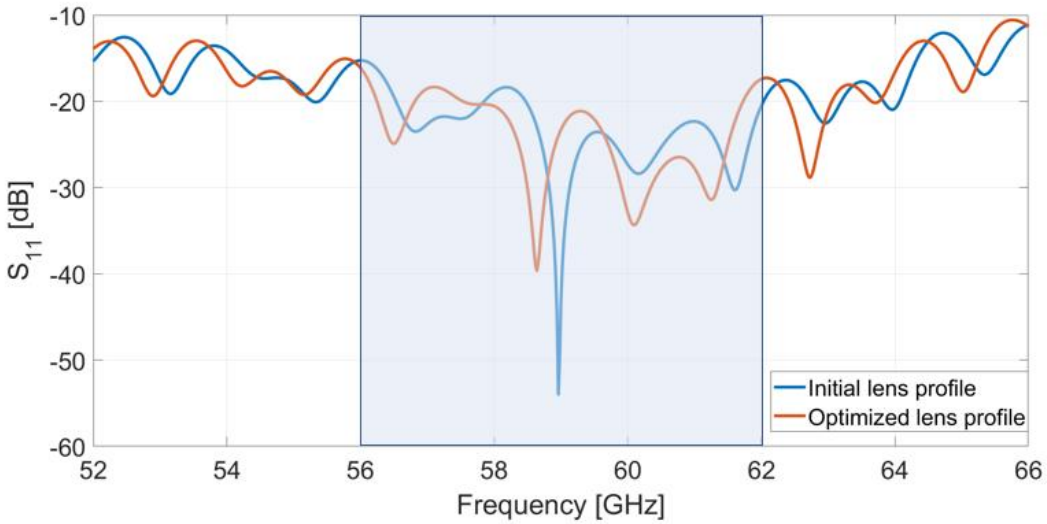

Figure 30: Comparison between S_{11} reflection coefficient of both the initial lens profile and the optimized lens profile.

3.9 MULTIPORT DOUBLE LAYER LENS LAYOUT AND RESULTS

Based on single port design, a multiport double layer nearfield geodesic lens has been designed and simulated. Figure 31 and Figure 32 show the vacuum part and metal part of the full lens. The flare, mirror and feeding designs, previously explained, have been exploited in this multiport design.

Figures 31 (a)-(b) depict a perspective view of the metal part of the double layer lens and its cross section view. On the contrary, Figure 32 (a)-(b) depict a perspective view of the air part and a top view showing the spacing between the ports and the aperture angle of the flare.

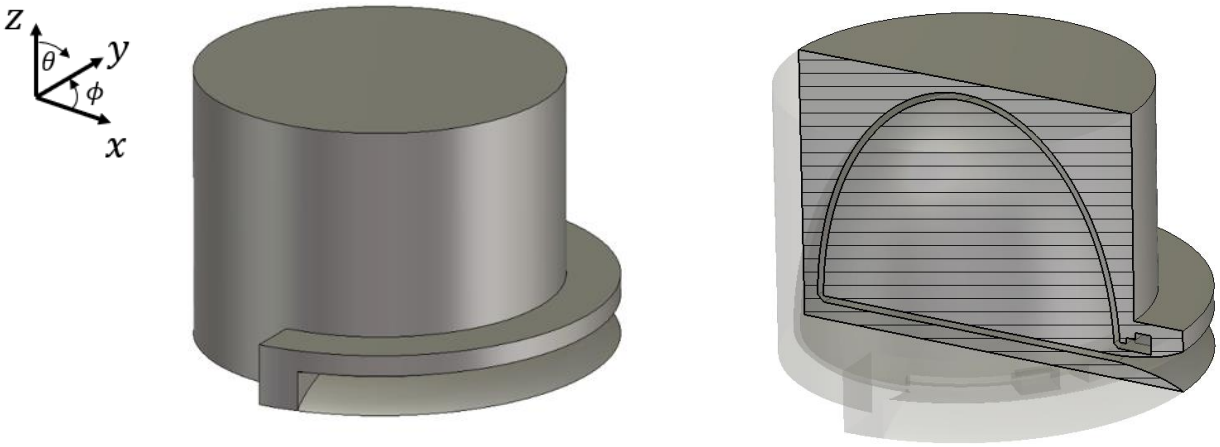

(a) (b)

Figure 31: Perspective view metal part (a) of double layer lens antenna and cross section view (b).

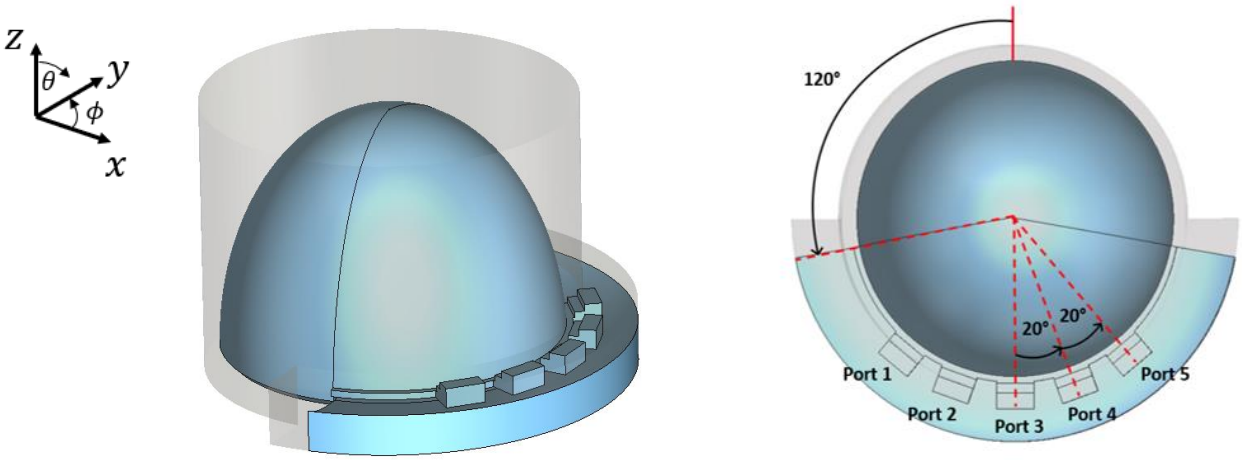

(a) (b)

Figure 32: Perspective view air part (a) of double layer lens antenna and top view (b).

The beamforming network is made of five uniformly spaced ports that allows a scanning range of $\pm 55°$. The choice of uniform spacing between the ports is led by the needed roll-off less than $3\ \mathrm{dB}$ at crossover points between the beams to improve beam coverage. Fur such purposes, the distance between the ports is adjusted accordingly.

Figures 33, 34 and 35 report the radiation patterns at the three different frequencies when all five ports are excited thus showing significant improvement in beam coverage obtained with such multiport nearfield focusing geodesic lens antenna.

Furthermore, a comparison between the multiport results in the case of initial lens profile (dashed) and optimized (solid) one is also reported. Indeed, from the radiation pattern plots, it's clear the need of optimization of the nearfield lens antenna since an $\mathrm{HPBW\ smaller\ than}\ 20°$ (dashed results) would have led to a roll-off equal to $7\ \mathrm{dB}$ between the beams resulting in poor performance beam coverage.

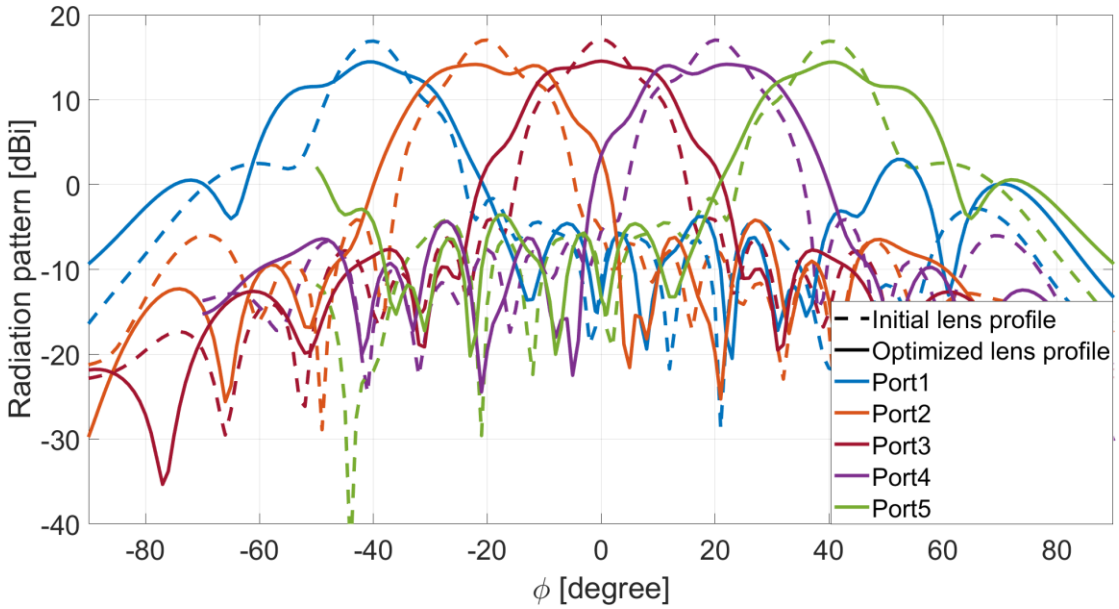

Figure 33: Radiation patterns at 56 GHz when all ports being fed both for the initial lens profile (dashed lines) and optimized lens profile (solid line).

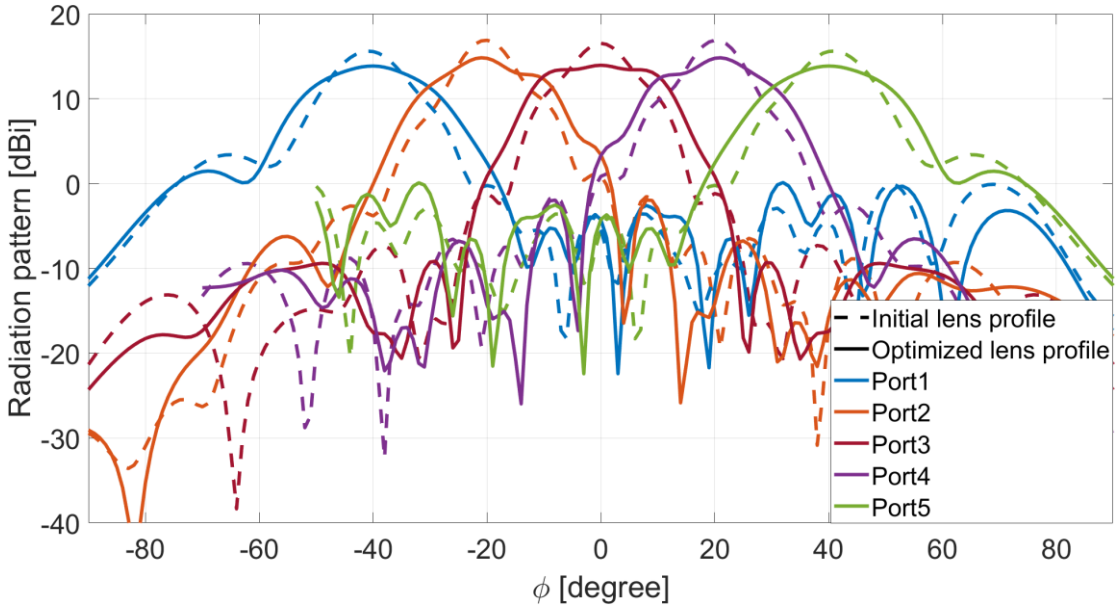

Figure 34: Radiation patterns at 60 GHz when all ports being fed both for the initial lens profile (dashed lines) and optimized lens profile (solid line).

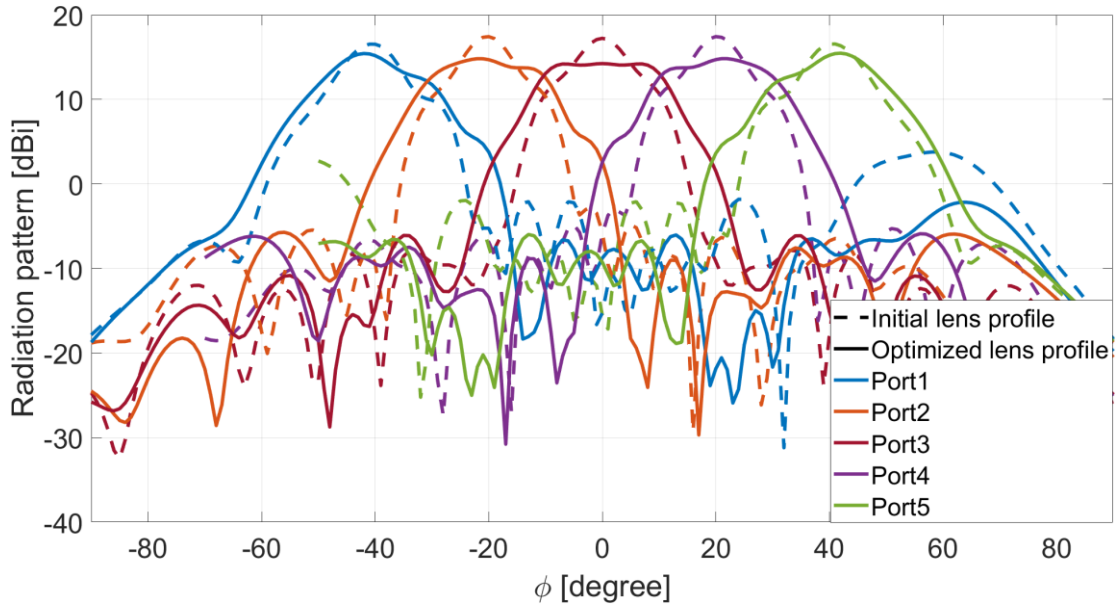

Figure 35: Radiation patterns at 62 GHz when all ports being fed both for the initial lens profile (dashed lines) and optimized lens profile (solid line).

As denoted from Figures 33-35, there are no scan losses and the achievable scanning range is equal to $\pm 55°$. Moreover, the requirement on the HPBW greater than $20°$ is satisfied at the center and at the extremes of the frequency band. The beam coverage has been improved since the roll-off between the beams at crossover points is less than $3\ \mathrm{dB}$ in order to have a stable aggregate gain over a wide scanning range. Below is reported the absolute value of the electric field $\vec{E}$ when feeding Port3 and Port1 at the frequencies of interest ($f_{min} = 56\ \mathrm{GHz}, f_c = 60\ \mathrm{GHz}, f_{max} = 62\ \mathrm{GHz}$) :

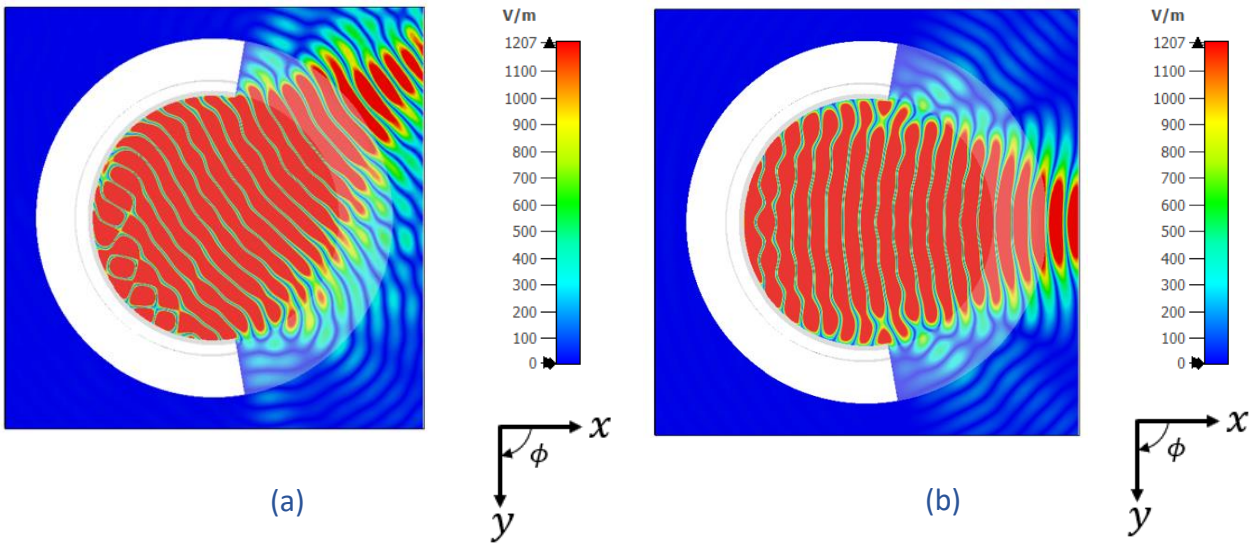

Figure 36: Absolute value of $\vec{E}$ at 56 GHz bottom view when Port1 (a) and Port3 (b) being fed.

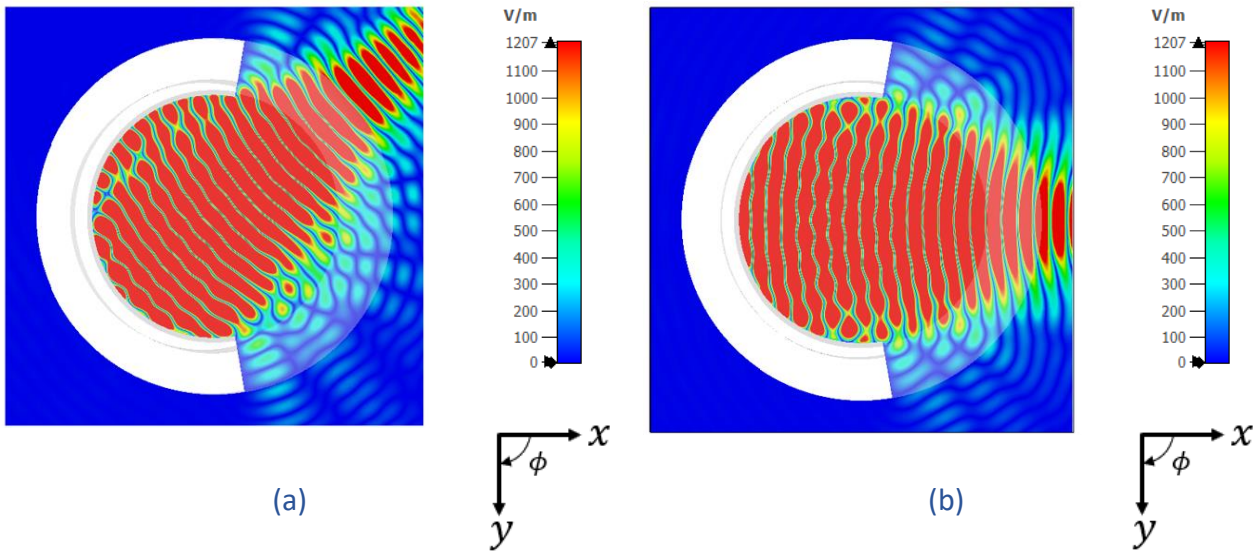

Figure 37: Absolute value of $\vec{E}$ at 60 GHz bottom view when Port1 (a) and Port3 (b) being fed.

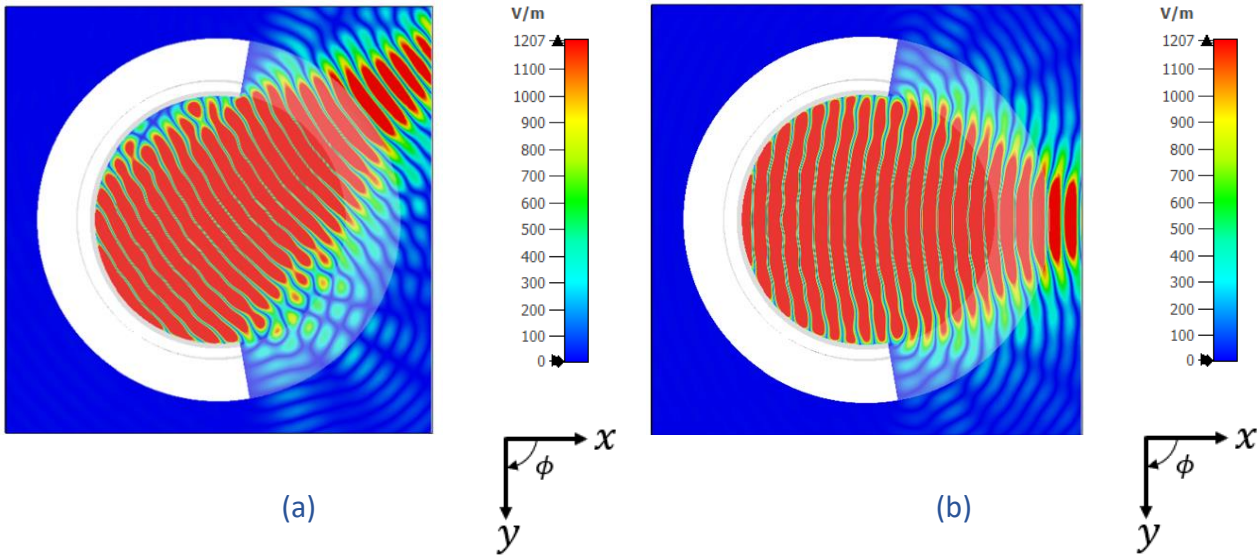

Figure 38: Absolute value of $\vec{E}$ at 62 GHz bottom view when Port1 (a) and Port3 (b) being fed.

The phase of the electric field $\vec{E}$ when feeding Port1-3 at the frequencies of interest ($f_{min} = 56$ GHz, $f_c = 60$ GHz, $f_{max} = 62$ GHz) is reported as well.

The phase fronts typical of a nearfield lens antenna are clearly outlined from the figures reported below.

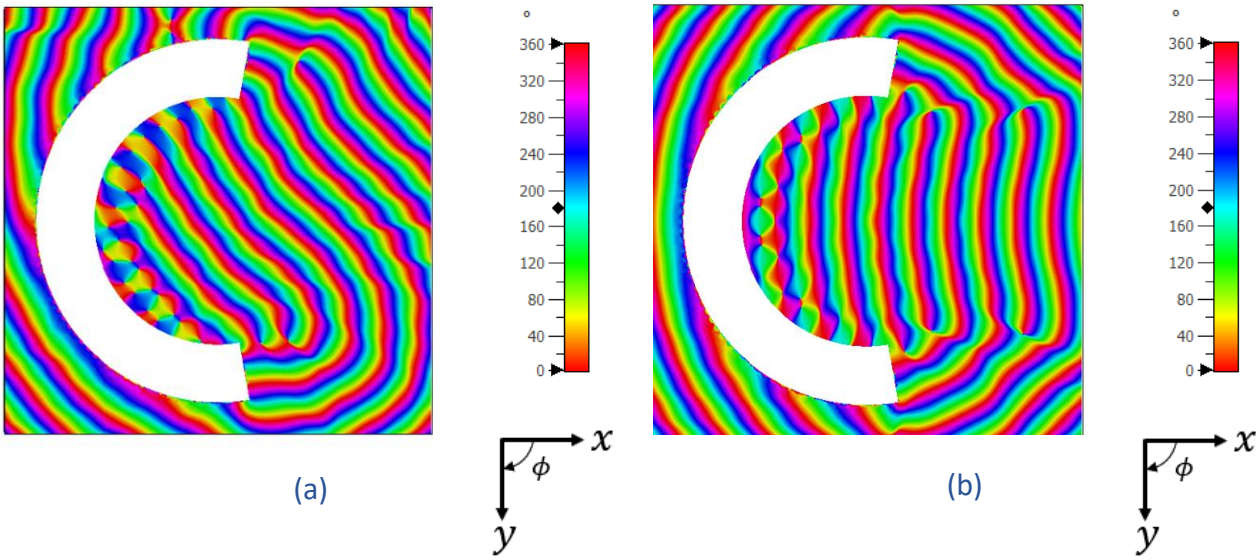

Figure 39: Phase of $\vec{E}$ at 56 GHz bottom view when Port1 (a) and Port3 (b) being fed.

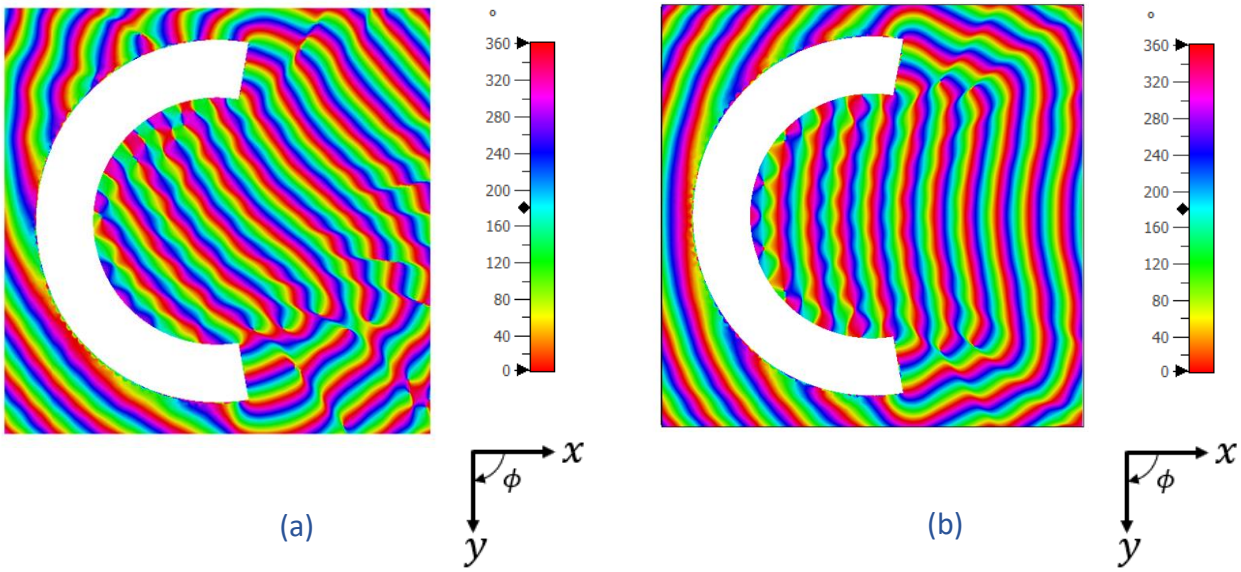

Figure 40: Phase of $\vec{E}$ at 60 GHz bottom view when Port1 (a) and Port3 (b) being fed.

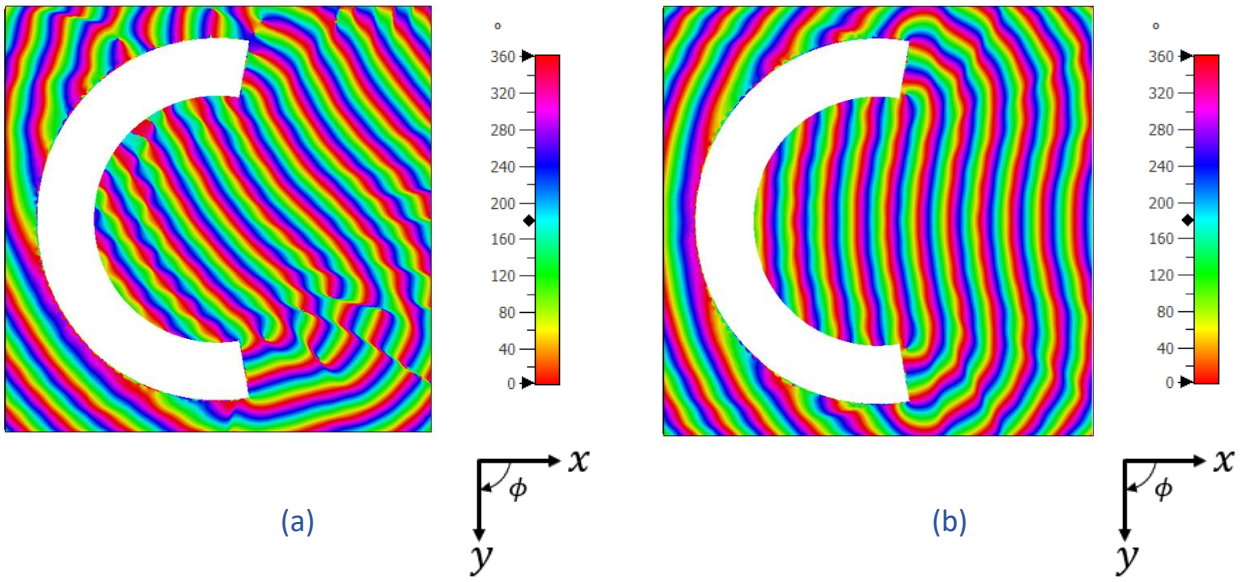

Figure 41: Phase of $\vec{E}$ at 62 GHz bottom view when Port1 (a) and Port3 (b) being fed.

From the previous reported electric field simulation results, it's evident the nearfield focusing property of the multiport double layer nearfield geodesic lens antenna (along all the frequency band and for scanning range $\pm 55°$). The reflection coefficients when Port1-5 being fed are reported below:

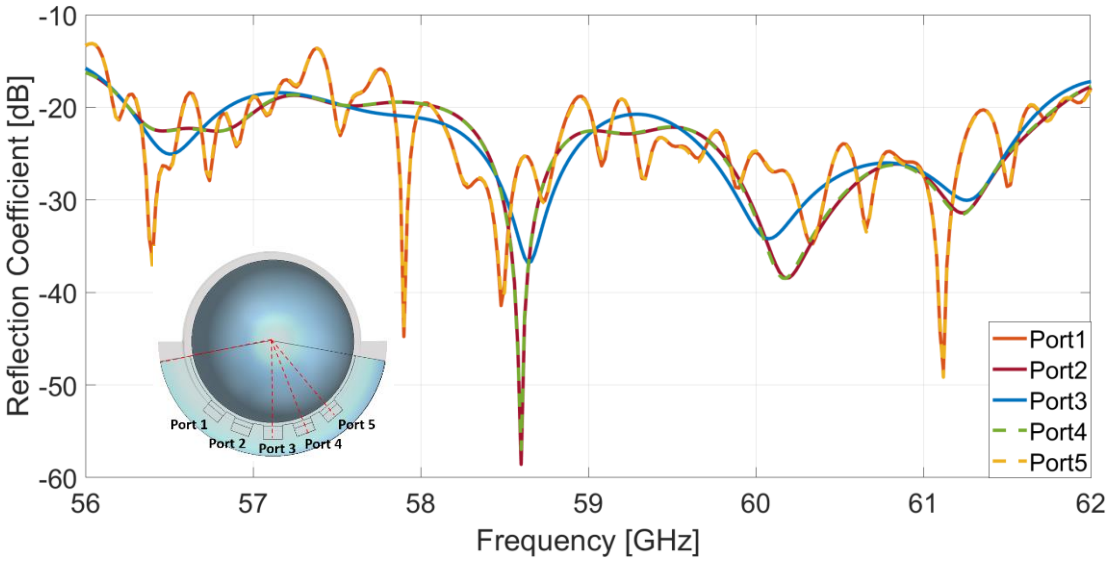

Figure 42: Reflection coefficient when Port1-5 being fed.

The reflection coefficients when Port2-4 being fed are all below $-15\ \mathrm{dB}$ in the frequency band $56-62\ \mathrm{GHz}$ whereas when Port1 and Port5 are fed the reflection coefficient is lower than $-12\ \mathrm{dB}$ thus achieving good impedance matching even when exciting extremes ports such as Port1 and Port5. Moreover, as it is depicted in Figure 42, the reflection coefficients S_{11}, S_{22} are equal to the reflection coefficients S_{44}, S_{55} since all the ports are symmetrically placed around Port3 and the lens has a rotationally symmetric property. S-parameters including coupling coefficients when Port3 being fed have been analyzed as well. Figure 43 reports the simulated results:

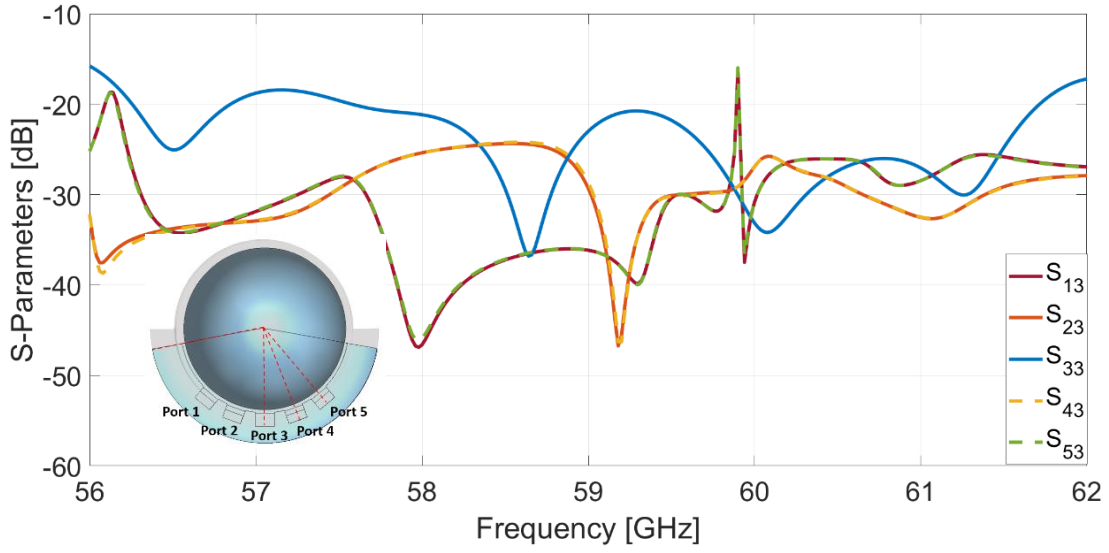

Figure 43: S-Parameters when Port3 being fed.

As it is depicted in Figure 43, the coupling coefficients S_{13}, S_{23} are equal to the coupling coefficients S_{43}, S_{53} due to the rotationally symmetric property.

The coupling coefficients are all below -15 dB when Port3 being fed in the frequency band $56 - 62$ GHz.

Moreover, S-parameters when Port1 being fed are also reported below:

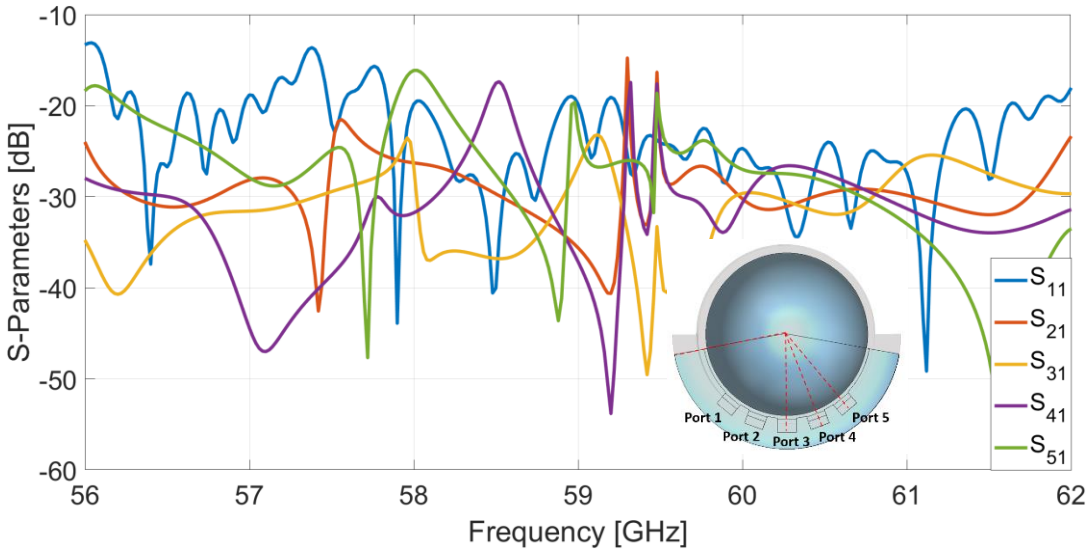

Figure 44: S-Parameters when Port1 being fed.

When feeding Port1, as previously mentioned, the reflection coefficient is lower than -12 dB in the frequency band of interest $56 - 62$ GHz whereas all the coupling coefficients, when Port1 being fed, are below -14 dB in $56 - 62$ GHz band thus showing low coupling between the ports of the lens antenna.

4 CONCLUSION AND FUTURE WORK

In this work a multiport double layer nearfield focusing geodesic lens has been implemented. As initial design, the lens profile obtained from the differential equation has been implemented showing poor performance in terms of beam coverage with a roll-off equal to $7\ \mathrm{dB}$ at cross over points between the beams and HPBW smaller than 20°. As a final design an optimization on the lens profile has been performed. Indeed, enhanced beam coverage characteristics and stable aggregate gain have been achieved thanks to the nearfield focusing property of the optimized lens. The gain roll-off is less than 3 dB at crossover points between the beams and the $\mathrm{HPBW}\ \mathrm{greater\ than}\ 20°$ thus satisfying the design requirements. The reflection and coupling coefficients have been analyzed thus showing good impedance matching and low coupling between the ports. Five uniformly spaced ports are fed to achieve a scanning range equal to $\pm\ 55°$ in H plane with good performance in the frequency band of interest.

Future work will include implementation and optimization of the coaxial-to-waveguide transition in order to feed the lens from the top of the structure. Moreover the manufacturing of the double layer nearfield geodesic lens and measurement of its performance to validate the CAD model built in the simulator should be performed. Improvement could be done in terms of reflection coefficients when feeding Port1 and Port5 thus reducing even more the roll-off between the beams and leading to further beam coverage.

Moreover, a folding method could be applied to lower the height of the double layer lens profile and reduce bulkiness of the full lens. As a consequence, a folded version of the initial unfolded lens reported in this work could be designed and simulated with the same design requirements but with a more compact footprint.

References

[1] Ericsson, “5G Wireless Access: An Overview” , Apr.2020.

[2] Ericsson, “Ericsson Mobility Report, Nov.2020.

[3] J.Zhang, X.Ge, Q.Li, M.Guizani, and Y.Zhang, “5G millimeterwave antenna array: Design and challenges”, IEEE Wireless Communications, vol. 24, no. 2, pp. 106–112, Apr. 2017.

[4] M.H.Dahri, M.Inam, M.H.Jamaluddin, and M.R.Kamarudin, “A review of high gain and high efficiency reflectarrays for 5G communications”, IEEE Access, vol. 6, pp. 5973–5985, 2018.

[5] O.Quevedo-Teruel, M.Ebrahimpouri, and F.Ghasemifard, “Lens antennas for 5G communications systems”, IEEE Communications Magazine, vol. 56, no. 7, pp. 36–41, Jul. 2018.

[6] F.Doucet, N.J.Fonseca, E.Girard, H.Legay, and R.Sauleau,“Analytical model and study of continuous parallel plate waveguide lens-like multiple-beam antennas”, IEEE Transactions on Antennas and Propagation, vol. 66, no. 9, pp. 4426–4436, 2018.

[7] Y.J.Cheng, W.Hong, K.Wu, Z.Q.Kuai, C.Yu, J.X.Chen, J.Y.Zhou, H.J.Tang, "Substrate Integrated Waveguide (SIW) Rotman Lens and Its Ka-Band Multibeam Array Antenna Applications", IEEE Transactions on Antennas and Propagation, vol. 56, no. 8, pp. 2504-2513, Aug. 2008.

[8] C.Pfeiffer and A.Grbic, “A printed, broadband Luneburg lens antenna”, IEEE Transactions on Antennas and Propagation, vol. 58, no. 9, pp. 3055–3059, Sep. 2010.

[9] O.Orgeira, G.Leòn, N.J.G.Fonseca, P.Mongelos, and O.Quevedo-Teruel, “Near-Field Focusing Multibeam Geodesic Lens Antenna for stable aggregate gain in Far-field”, IEEE Transactions on Antennas and Propagation, vol. 70, no. 5, pp. 3320–3328, May 2022.

[10] C.A.Fernandes, E.B.Lima, and J.R.Costa, “Dielectric Lens Antennas,” Handbook of Antenna Technologies, pp. 1001–1064, 2016.

[11] J.Ruiz Garcia, E. Martini,C.Giovampaola , D.González-Ovejero and S.Maci, “Reflecting Luneburg lenses “, IEEE Transactions on Antennas and Propagation, pp.3924-3935, 2021.

[12] X.Fu, F.Yang, C.Liu, X.Wu, and T.J.Cui, “Terahertz Beam Steering Technologies: From Phased Arrays to Field-Programmable Metasurfaces”, Advanced optical Materials, vol.8, Aug. 2008.

[13] F.Fan, M.Cai, J.Zhang, Z.Yan and J.Wu, "Wideband Low-Profile Luneburg Lens Based on a Glide-Symmetric Metasurface", IEEE Access, vol. 8, pp. 85698-85705, 2020.

[14] K.Wu, M.Bozzi, and N.J.G.Fonseca, “Substrate integrated transmission lines: Review and applications”, IEEE Journal of Microwaves, vol. 1, no. 1, pp. 345–363, Jan. 2021.

[15] Rinehart RF, Journal of Applied Physics 19, 860-852, 1948.

[16] M.Šarbort and T.Tyc , “Spherical media and geodesic lenses in geometrical optics”, Journal of Optics, vol. 14, no. 7, Jul. 2012.

[17] W.Rotman, "Wide-angle scanning with microwave double-layer pillboxes," IEEE Transactions on Antennas and Propagation, vol. 6, no. 1, pp. 96-105, Jan. 1958.

[18] Q.Chen, S.A.Horsley, N.J.Fonseca, T.Tyc, and O.Quevedo-Teruel, “Double-layer geodesic and gradient-index lenses,” Nature Communications, vol. 13, no. 1, pp. 1–12, 2022.

[19] Q.Chen, S.A.R.Horsley, N.J.G.Fonseca, T.Tyc and O.Quevedo-Teruel, "A General Solution for Double-Layer Gradient-Index and Geodesic Lenses with Rotational Symmetry," IEEE Transactions on Antennas and Propagation, pp. 1-5,2023.

[20] K.Tekkouk, J.Hirokawa, R.Sauleau, and M.Ando, “Wideband and large coverage continuous beam steering antenna in the 60-GHz band,” IEEE Transactions on Antennas and Propagation, vol. 65, no. 9, pp. 4418–4426, 2017.

[21] A.Gomez-Torrent, M.Garcıa-Vigueras, L.Le Coq, A.Mahmoud, M.Ettorre, R.Sauleau, and J. Oberhammer, “A low-profile and high gain frequency beam steering subterahertz antenna enabled by silicon micromachining,” IEEE Transactions on Antennas and Propagation ,vol. 68, no. 2, pp. 672–682, 2020.

[22] P.Castiillo-Tapia, O.Zetterstrom, A. Algaba-Brazalez, L.Manholm, M.Johansson, N.J.G.Fonseca and O.Quevedo-Teruel, "Two-Dimensional Beam Steering Using a Stacked Modulated Geodesic Luneburg Lens Array Antenna for 5G and Beyond", IEEE Transactions on Antennas and Propagation, vol. 71, no. 1, pp. 487-496, Jan. 2023.